



# HAMSOM-VICE v0.9: Comparison of two variable ice-ocean drag coefficient parameterizations on annual simulations of Bohai Sea ice

Libang Xu<sup>1</sup>, Bin Jia<sup>1</sup>, Yu Liu<sup>1</sup>, Xue'en Chen<sup>2</sup>, Donglin Guo<sup>3</sup>

<sup>1</sup>Marine Science and Technology College, Zhejiang Ocean University, Zhoushan, 316000, China

<sup>2</sup>College of Oceanic and Atmospheric Sciences, Ocean University of China, Qingdao, 266000, China

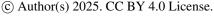
<sup>3</sup>North China Sea Marine Forecasting and Hazard Mitigation Center of Ministry of Natural Resources, Qingdao, 266000, China

Correspondence to: Bin Jia (2022172@zjou.edu.cn)

**Abstract.** This study compares the simulation performance of two ice-ocean drag coefficient parameterizations (Schemel (original scheme): large-scale roughness parameterization, Scheme2 (newly introduced scheme): small-scale geometric roughness parameterization) for the Bohai sea ice in the 2011/2012 ice season, revealing main component of the ice-ocean drag coefficient ( $C_{dw}$ ) and its crucial regulatory role in sea ice dynamic-thermodynamic processes in the Bohai Sea. The findings demonstrate that, for the ice-ocean drag in the thin ice environment of the Bohai Sea, the ice-bottom surface skin drag and the ice floe edge form drag dominate, while the contribution of ice keel-related drag is negligible due to insufficient ice thickness (averaging 20-30 cm). Scheme2 reduces the root mean square error (RMSE) of daily total ice area by 28 % compared to the Scheme1, showing higher simulation accuracy in the overall spatiotemporal ice evolution in the Bohai Sea. While Scheme1 demonstrates closer agreement with the observed length of ice season (underestimating by only 7 days). The result analysis of key sea ice variables and ice-ocean interfacial variables indicates that  $C_{dw}$  can affect the ice velocity through the dynamic feedback mechanism, and the basal freezing/melting through the thermodynamic dual feedback mechanisms.

## 1 Introduction

The Bohai Sea is a semi-enclosed continental shelf sea in northern China with a maximum depth of no more than 70 m, which has rich fishery resources and oil and gas resources. It is also one of the lowest-latitude seas covered by natural sea ice (Su et al., 2004). Annual winter, driven by cold fronts and Arctic air masses, variable sea ice coverage across the region. The main ice extents in the Bohai Sea include Liaodong Bay, Bohai Bay and Laizhou Bay. The sea ice is predominantly first-year ice with an average thickness of 20-30 cm, though extreme cold events can produce ice up to 60 cm thick. The ice season lasts from mid to late November to the end of February or early March of the following year, lasting for about 4 to 5 months (Shi et al., 2019). The winter ice conditions have historically posed substantial challenges to maritime operations and coastal economies in the Bohai Sea (Zhang and Yue, 2011; Gu et al., 2013; Ning et al., 2018; Guo et al., 2019; Yan et al., 2019). Currently, numerical modelling of sea ice is a crucial tool for predicting the freeze, melt, and drift patterns of sea ice in the Bohai Sea (Su et al., 2005).







In numerical simulation of sea ice, the ice dynamic behavior, such as drifting, deformation, and mechanical strength, is governed by internal stresses and the input of external momentum flux from wind forces and ocean currents. The ice-ocean drag coefficient C<sub>dw</sub> is a critical coefficient, which governs momentum and kinetic energy exchange at the ice-ocean interface, ultimately influencing the transport of momentum and heat fluxes between sea ice and the underlying ocean (Martinson and Wamser, 1990; Castellani et al., 2018; Kawaguchi et al., 2024; Sterlin et al., 2023; Tsamados et al., 2014; Cole et al., 2017).
Its magnitude depends on factors such as ice bottom roughness, turbulent mixing in the mixed layer, and sea ice coverage status (e.g., ice thickness) (Mai et al., 1996; Harder, 1997; Overland and Colony, 1994; Overland and Davidson, 1992). Empirical measurements of ice-ocean drag coefficient C<sub>dw</sub> have predominantly focused on the Arctic Ocean and its marginal seas, yielding regional specific values. Table 1 summarizes observed ice-ocean drag coefficients referenced to their measurement depth levels. These observations provide a good reference for the C<sub>dw</sub> value in the sea ice model.

40 Table 1: The comparison table of ice-ocean drag coefficient (GSC represents the depth of geostrophic current).

Region	Depth (m)	Drag Coefficient (× 10 <sup>-3</sup> )	Ice Type	Reference
Beaufort Sea (AIDJEX)	-	3.4	1 km Smooth Ice Floe	Mcphee and Smith (1976)
Beaufort Sea (AIDJEX)	1	2.0	-	Mcphee (1979)
Bering Sea	1.1	14.1	30 m Rough Ice Floe	Madsen and Bruno (1987)
Bering Sea	1.1	24.2	Rough Ice Floe	Pease et al. (1983)
Weddell Sea	GSC	1.13	-	Martinson and Wamser (1990)
Gulf of St. Lawrence	0.5	47	10 m Rough Ice Floe	Johannessen (1970)

In order to describe the ice-ocean dynamic process more accurately, the determination of the ice-ocean drag coefficient has gradually been replaced by parameterizations instead of empirical constants. An approach for parameterizing the ice-ocean drag coefficient find a way in the large-scale roughness feature, the deformation energy (R), by establishing a directly relationship between the drag coefficient and deformation energy R with other sea ice variables (Steiner, 2001; Steiner et al., 1999). This scheme parameterizes the ice-ocean drag coefficient as a binary function of ice concentration  $(A_i)$  and deformation energy (R), and containing both form drag and skin drag simultaneously, which had adopted by the ice module we used and also demonstrated strong performance in Arctic sea ice simulations (Steiner, 2001; Steiner et al., 1999).

In addition, the ice-ocean drag coefficient parameterization can also draw on the air-ice drag coefficient parameterization. Arya (1975, 1973) divided the air-ice drag into form drag induced by the sea ice small-scale roughness features (e.g., ice sails and keels) and skin drag generated by the air-ice intermediate transition layer. Further, the form drag caused by ice floe edges was also quantified and taken into account in the parameterization scheme by Hanssen-Bauer and Gjessing (1988). Therefore, another ice-ocean drag coefficient parameterization developed by Lu et al. (2011) and Tsamados et al. (2014), partitions the ice-ocean drag coefficient into three components: skin drag, form drag induced by ice keels, and form drag from floe edges,

which are induced by the sea ice small-scale roughness features.

55

https://doi.org/10.5194/egusphere-2025-4290 Preprint. Discussion started: 20 November 2025

© Author(s) 2025. CC BY 4.0 License.





Although the parameterizations of ice-ocean drag coefficient have made long time progress, there are still few studies on the comparison of the effects of parameterizations based on different ice roughness features. At the same time, research on the ice-ocean drag coefficient in the Bohai Sea is still rare, given the Bohai Sea's shallow bathymetry and the prevalence of thin, fragile ice, region-specific optimization of dynamic parameters like  $C_{dw}$  could be essential for improving the accuracy of short-term sea ice simulations in the Bohai Sea. At present, in the numerical simulation studies of the Bohai Sea ice,  $C_{dw}$  is always set as a constant value. Ji (2001) calculated the ice-ocean drag coefficient in the Liaodong Bay area of the Bohai Sea by using the momentum method based on the ice drift trajectory measured and tracked by radar (the value was approximately  $2.6 \times 10^{-3}$ ). Su et al. (2003) empirically set the ice-ocean drag coefficient to  $4.5 \times 10^{-3}$  in their numerical simulation study of interfacial thermal equilibrium of Bohai sea ice.

To explore the applicability and benefits of ice-ocean drag coefficient parameterization in the simulation of sea ice in the Bohai Sea, the two ice-ocean drag coefficient parameterization schemes mentioned above are introduced in the Bohai Sea ice dynamics module in this paper. The first scheme (Scheme1, also the original scheme in the coupled model) is the one proposed by Steiner et al. (1999) and Steiner (2001), incorporates sea ice internal forces and links them to a simulated large-scale sea ice roughness variable—the deformation energy (R). The ice-ocean drag coefficient is then parameterized as a linear function of R combined with a quadratic dependence on ice concentration ( $A_i$ ). In contrast, we have revised the model by implementing a newly introduced scheme (Scheme2) which decomposes the ice-ocean drag coefficient into skin drag, ice ridge (keel) form drag and floe edge form drag, and directly calculates each drag coefficient based on grid-resolved small-scale roughness features, specifically the average keel depth (Steiner et al., 1999; Tsamados et al., 2014). The specific introductions of the two parameterization schemes are detailed in the appendix.

The model and data used in this study are described in section 2. Section 3 compares the ice-ocean drag coefficients and spatiotemporal distribution differences of sea ice variables between the two parameterization schemes, systematically analysed their thermodynamic and dynamic output variables, and elucidates the causes of these differences. Finally, section 4 summarizes the research findings and conclusions for both parameterization schemes.

#### 2 Model and data

# 2.1 Model description

We conducted numerical simulations of Bohai Sea ice using a coupled ice-ocean model HAMSOM-VICE v0.9 which combines the Hamburg Shelf Ocean Model (HAMSOM) with a sea ice model called Vector Ice Model (VICE). HAMSOM is a baroclinic three-dimensional model developed at the University of Hamburg (Backhaus, 1985; Backhaus, 2008), which adopts a semi-implicit scheme formulated for the "Arakawa C grid" for the numerical solution of the shallow water equations (Backhaus, 1983). The sea-ice model is a modification of the viscous-plastic model suggested by Hibler (1979) with three layer thermodynamics according to Semtner (1976). The model generally accounts for dynamic and thermodynamic processes



105



in both sea ice and open water using an isotropic viscous-plastic rheology. The vertical structure of the sea ice consists of three ice layers and a snow layer, and it is governed by the momentum equation and a one-dimensional heat diffusion equation (Hibler, 1979). The fundamental sea ice equations, thermodynamic properties, and rheology were introduced in detail by Ólason and Harms (2010) and Olason (2016). The HAMSOM and VICE were coupled and developed at the University of Hamburg around 2011-2016. This coupled model was successfully applied to numerical simulations of sea ice in the Kara Sea, a marginal sea of the Arctic Ocean, demonstrating good performance (Olason, 2016). Subsequently, we applied this coupled model to the study of sea ice in the Bohai Sea, conducting a series of adjustments and improvements to better suit the regional conditions (Jia and Chen, 2020; Jia et al., 2022; Jia et al., 2024).

95 The schematic diagram of the model coupled structure is shown in Fig. 1.

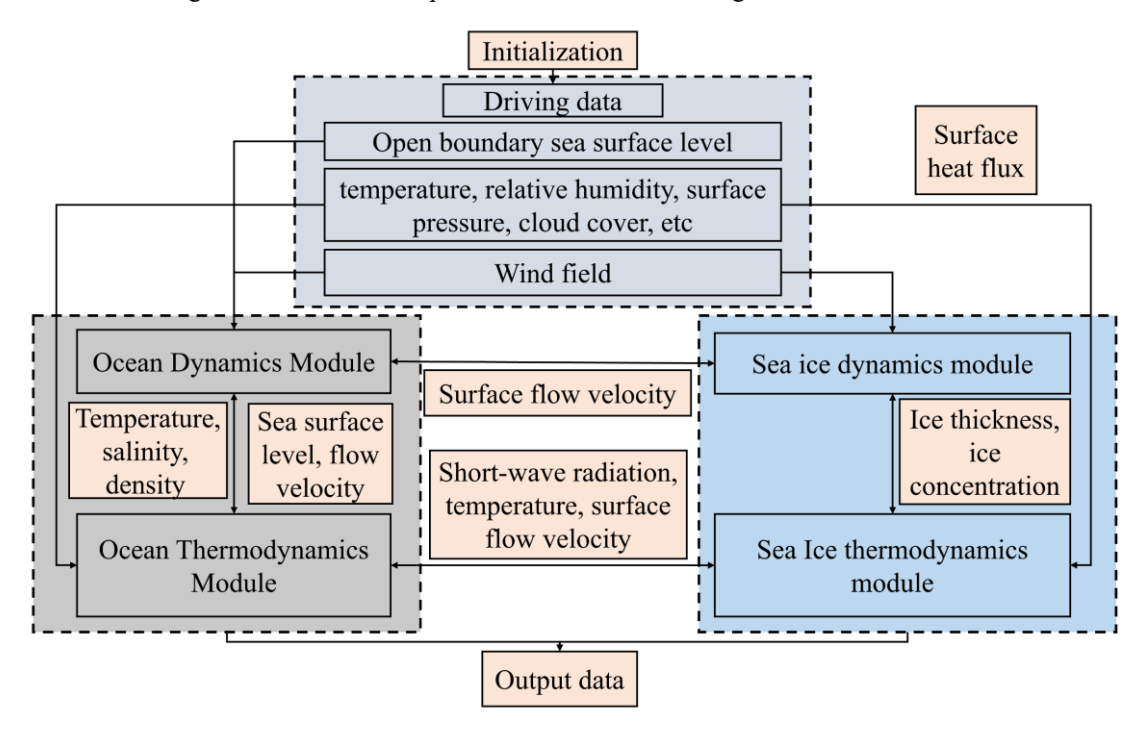


Figure 1: Schematic diagram of the coupled structure of ocean model and sea ice model.

As we can see, the ocean model and sea ice model are coupled through the interaction of various modules. The process begins with initialization and driving data, including meteorological inputs such as wind fields, shortwave radiation, temperature, and humidity, which provide boundary conditions and initial states for both the ocean and sea ice modules. The coupling operates bidirectionally: the Ocean Dynamics Module outputs sea surface height and current velocity, directly influencing the Sea Ice Dynamics Module, which determines ice movement and distribution (e.g., thickness and concentration). Meanwhile, temperature and salinity from the Ocean Thermodynamics Module affect the Sea Ice Thermodynamics Module via surface heat flux, regulating ice growth or melt. In turn, the Sea Ice Module feeds back into the ocean system by altering surface heat exchange (e.g., shortwave radiation reflection) and frictional drag, modifying ocean dynamics. The coupled system ultimately





produces integrated outputs, including sea ice state (thickness, concentration), ocean state (temperature, current velocity, salinity), and heat flux, forming a closed-loop interaction.

The model simulation domain covers the Bohai Sea (37.0-41.25° N, 117.25-122.5° E, shown in Fig. 2), with a horizontal resolution of 1' (about 1.5km). In the vertical, the domain is divided into 12 levels, with thicknesses ranging from 6 meters at the surface to approximately 68 meters at depth. The simulated time period was from November 1, 2011 to March 31, 2012, covering the 2011/2012 ice season, with a time step of 60 seconds.

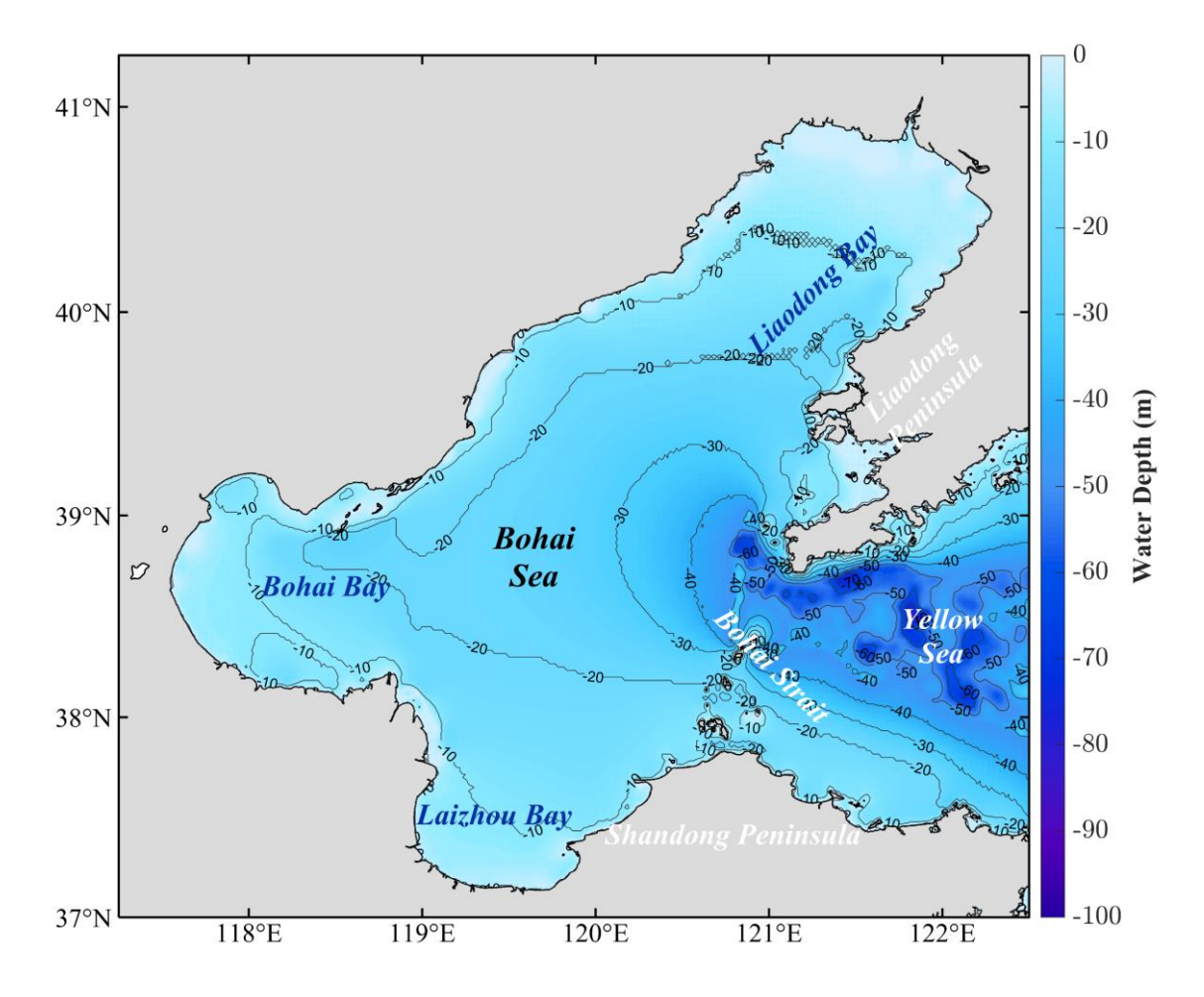


Figure 2: Topographic map of Bohai Sea, three bays (Liaodong Bay, Bohai Bay, Laizhou Bay) and Bohai Strait.

# 2.2 Data description

#### 2.2.1 Model input data

115

The topographic data was provided by the North Sea Branch of the Ministry of Natural Resources, underwent high-precision interpolation, and was shoreline-calibrated. The initial temperature field was initialized using fusion temperature data

https://doi.org/10.5194/egusphere-2025-4290 Preprint. Discussion started: 20 November 2025

© Author(s) 2025. CC BY 4.0 License.



120

130

135

140



constructed by the Simple Ocean Data Assimilation (SODA) dataset (Carton et al., 2018) and high-resolution satellite remote sensing assimilation SST (Group for High-Resolution Sea Surface Temperature, GHRSST) (Donlon et al., 2012), using the "vertical projecting" assimilation method (Jia et al., 2022). The initial salinity field was interpolated from the 2018 World Ocean Atlas monthly climatological salinity field (Zweng et al., 2019).

The atmospheric forcing was derived from the hourly NCEP reanalysis dataset (Saha et al., 2011), which was spatially interpolated and includes the following surface parameters: 2 m air temperature, wind speed, cloud cover, precipitation rate, and specific humidity.

The initial elevation, initial current velocity and initial ice fields are set to zero. The harmonic constants of eight main tidal constituents at the open boundary are provided by The Oregon State University (OSU) Tidal Databases (Erofeeva et al., 2020).

#### 2.2.2 Observation data

The sea ice area observations derived from satellite remote sensing were provided by the North China Sea Marine Forecasting Center of the Ministry of Natural Resources. These observational data were used to evaluate the simulation effects of sea ice variables in the Bohai Sea of two parameterization schemes.

#### 3 Results and discussion

To systematically compare the differences in sea ice variables between parameterization Scheme1 and Scheme2 across various ice periods, and investigate the underlying mechanisms linking spatiotemporal variations of sea ice variables with drag coefficients, this study selects five representative days corresponding to the key periods of Bohai Sea ice seasonal evolution: initial ice period (Day 50, reflecting initial freezing characteristics), growth period (Day 70, representing rapid expansion), peak ice period (Day 90, demonstrating maximum ice conditions), melt period (Day 110, showing melting characteristics), and terminal ice period (Day 120, characterizing residual ice distribution). Through comparative analysis of key variables including ice concentration, thickness, and velocity, combined with satellite remote sensing data, we focus on examining how the ice-ocean drag coefficient  $C_{dw}$  regulates the dynamic and thermodynamic processes at the ice-ocean interface under different parameterization schemes, and to reveal the mechanistic impacts of parameterization differences on sea ice simulations. All figures were generated using the scientific colour maps 8.0 (Crameri, 2023) to ensure accessibility for readers with colour vision deficiency.

# 3.1 Drag coefficient distribution

Firstly, we conduct a comparative analysis of the ice-ocean drag coefficients calculated by the two parameterization schemes.



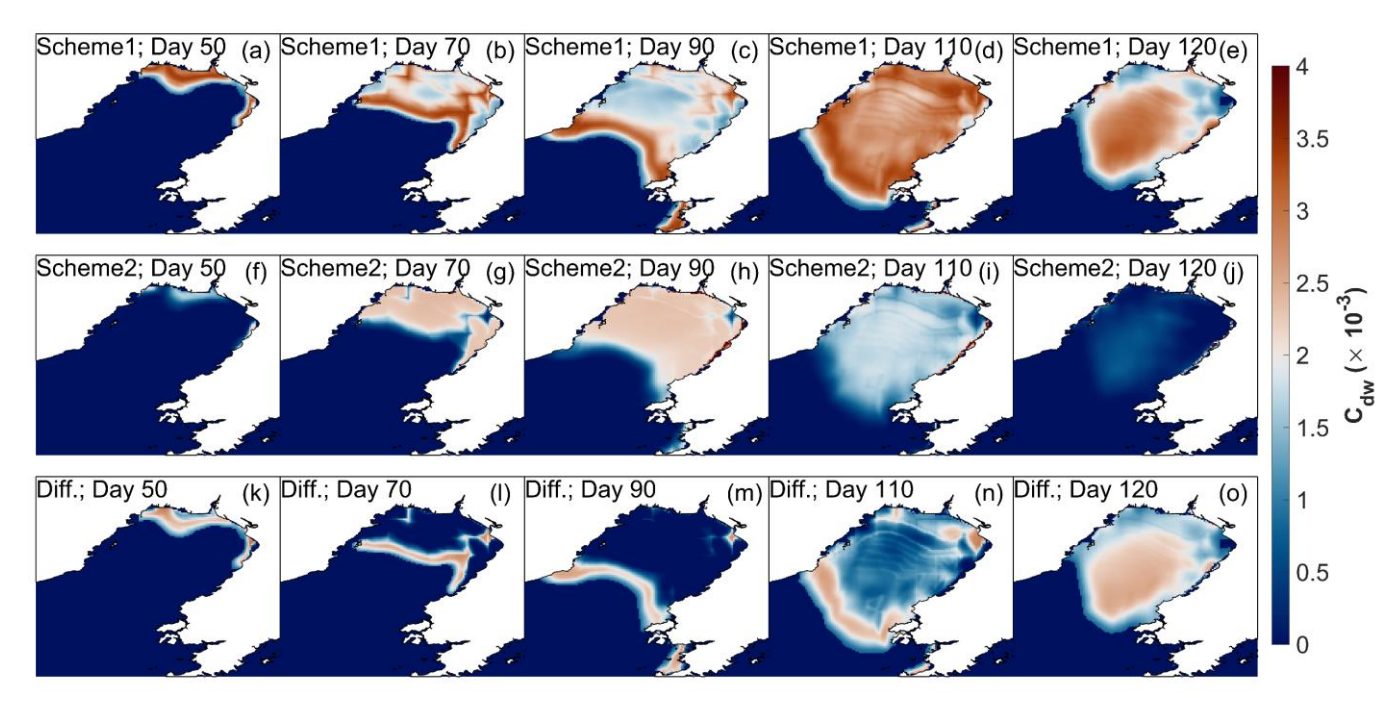
155

160



#### 145 3.1.1 Total ice-ocean drag coefficient

Figure 3 presents the total ice-ocean drag coefficient  $C_{dw}$  distributions simulated by two parameterization schemes on the five representative days. The results reveal significant differences in the evolution patterns of  $C_{dw}$  between the two schemes: Scheme 1 exhibits continuous expansion of  $C_{dw}$  coverage from the initial ice period to peak ice period, reaching its maximum in both spatial extent and magnitude during the melt period, then gradually decreasing in the terminal ice period. Whereas Scheme shows that  $C_{dw}$  peaks during the peak ice period and subsequently declines through the melt to terminal ice period. Regarding spatial distribution patterns, Schemel demonstrates a pronounced near edge-enhanced characteristics from initial ice period to melt period, with significantly higher drag coefficients (approximately  $3.0-4.0\times10^{-3}$ ) near the marginal ice zone (abbreviated as MIZ) compared to interior regions  $(1.0 - 2.5 \times 10^{-3})$ , but transitions to a center-high pattern during the terminal ice period. In contrast, Scheme2 maintains a consistent center-high and edge-low distribution pattern throughout. The central values (around  $2.5 \times 10^{-3}$ ) radial decrease to the edge. The difference fields (Scheme1 - Scheme2) indicate that the key distinction between the two parameterization schemes lies in Scheme 1's more developed  $C_{dw}$  magnitude in MIZ. However, from melt period onward, the discrepancies between Scheme1 and Scheme2 become increasingly pronounced. This behavior stems from Scheme 1's ice-ocean drag parameterization as a function of both ice concentration  $A_i$  and deformation energy R, specifically formulated through a linear proportionality to deformation energy combined with a parabolic dependence on ice concentration. Given that thin Bohai Sea ice generates relatively low deformation energy, ice concentration dominates the drag coefficient calculation. Consequently, the ice-ocean drag coefficient reaches its maximum in MIZ regions where ice concentration approaches 0.5.





170

180



Figure 3: The total drag coefficient  $C_{dw}$  distributions of Parameterization Scheme1 (3(a), 3(b), 3(c), 3(d), 3(e)), Parameterization Scheme2 (3(f), 3(g), 3(h), 3(i), 3(j)), and the difference between Scheme1 and Scheme2 (Scheme1-Scheme2) (3(k), 3(l), 3(n), 3(n), 3(o)) on the five representative days.

#### 3.1.2 Partial drag coefficients of Scheme2

In Scheme 2, the total ice-ocean drag coefficient is partitioned into three distinct components: skin drag  $C_{dw}^s$ , form drag induced by ice keels  $C_{dw}^r$ , and form drag from floe edges  $C_{dw}^f$ . To quantify their relative contributions in Bohai Sea ice simulations, we analysed the spatial distributions of these three drag coefficients during the five ice periods.

Figure 4 presents the spatial distributions of the floe edge form drag coefficient ( $C_{dw}^f$ ), the skin drag coefficient ( $C_{dw}^s$ ), and keel form drag coefficient ( $C_{dw}^r$ ) for five ice periods throughout the ice season in the Bohai Sea, simulated by Scheme 2. The results reveal that  $C_{dw}^f$  and  $C_{dw}^s$  exhibit highly similar spatiotemporal evolution patterns. Both intensify and expand outward from initial formation, peak in spatial coverage and magnitude during the peak ice period, then decay as the ice retreats toward the terminal period, collectively displaying a gradient distribution that decreases from the center towards the edge.  $C_{dw}^f$  primarily ranges between  $0-5\times 10^{-4}$ , whereas  $C_{dw}^s$  is significantly higher, with dominant values concentrated in the range of  $2.0-2.5\times 10^{-3}$ . It is particularly noteworthy that no significant distribution of the ice keel form drag coefficient ( $C_{dw}^r$ ) was observed in the Bohai Sea throughout the simulation period. This can be explained by the fact that the deformation energy R of the Bohai Sea ice is too small. In the Bohai Sea, whether in the edge areas or within the ice zones, due to the small deformation energy generated by thin ice, the ridge formation equation of keel involved by deformation energy R cannot yield real roots when calculating the height of the keel (for details, please see the appendix: Appendix A), thus no obvious ridge effect can be produced. The results confirm that, within the sea ice drag dynamics of the Bohai Sea, the surface form drag ( $C_{dw}^s$ ) plays a dominant role, with its contribution being approximately an order of magnitude greater than that of the floe-edge form drag ( $C_{dw}^f$ ).





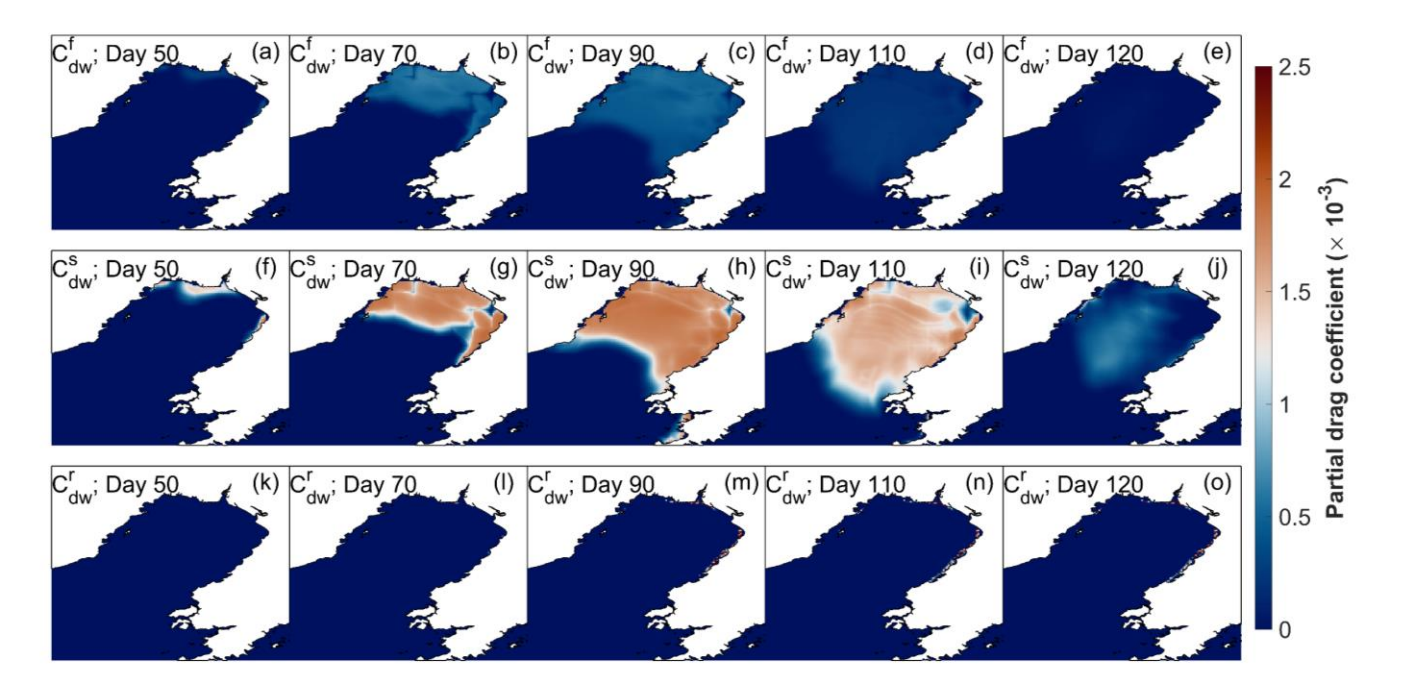


Figure 4: The distribution of three partial drag coefficients, ice floe edge form drag coefficient  $C^f_{dw}$  (4(a), 4(b), 4(c), 4(d), 4(e)), skin drag coefficient  $C^s_{dw}$ (4(f), 4(g), 4(h), 4(i), 4(j)), keel form drag coefficient  $C^r_{dw}$  (4(k), 4(l), 4(m), 4(n), 4(o)) of Scheme2 on the five representative days.

#### 3.2 Sea ice variables

185

200

To elucidate how spatiotemporal heterogeneity in ice-ocean drag coefficients influence sea ice simulations, we examined temporal evolution of total ice area and spatial distributions of ice thickness, concentration and velocities across the five ice periods. This period-segmented approach captures the ice-ocean drag coefficient-dependent feedback in different ice periods, to reveal how the influence of the drag coefficient manifests in the output results of key sea ice variables. As the vast majority of the sea ice in the 2011/2012 ice season was distributed in the Liaodong Bay, the spatial distribution of ice variables in the following text only shows the Liaodong Bay.

#### 3.2.1 Total ice area

The comparison of total ice area simulated by Scheme1 and Scheme2 and the observation data are shown in Fig. 5a. Observation data indicates that the Bohai Sea ice formation started on day 31 (December 1, 2011), reached maximum ice area ( $\approx 2 \times 10^4$ ) on day 101 (February 9, 2012), and subsequently melted completely by day 130 (March 10, 2012). It can be seen that the simulations of both schemes can capture the overall growth and decline evolution process of this ice season.

However, except for the peak period, both schemes slightly overestimated the total ice area compared to the satellite observations. The primary discrepancy emerges after day 111 (February 19, 2012), during the melt period, where Scheme2



210

215

220



exhibits a significantly faster decline in ice area than Scheme1 (Fig. 5b). This divergence becomes increasingly pronounced following the onset of melting, suggesting that inherent differences in the interfacial flux calculations between the two schemes.

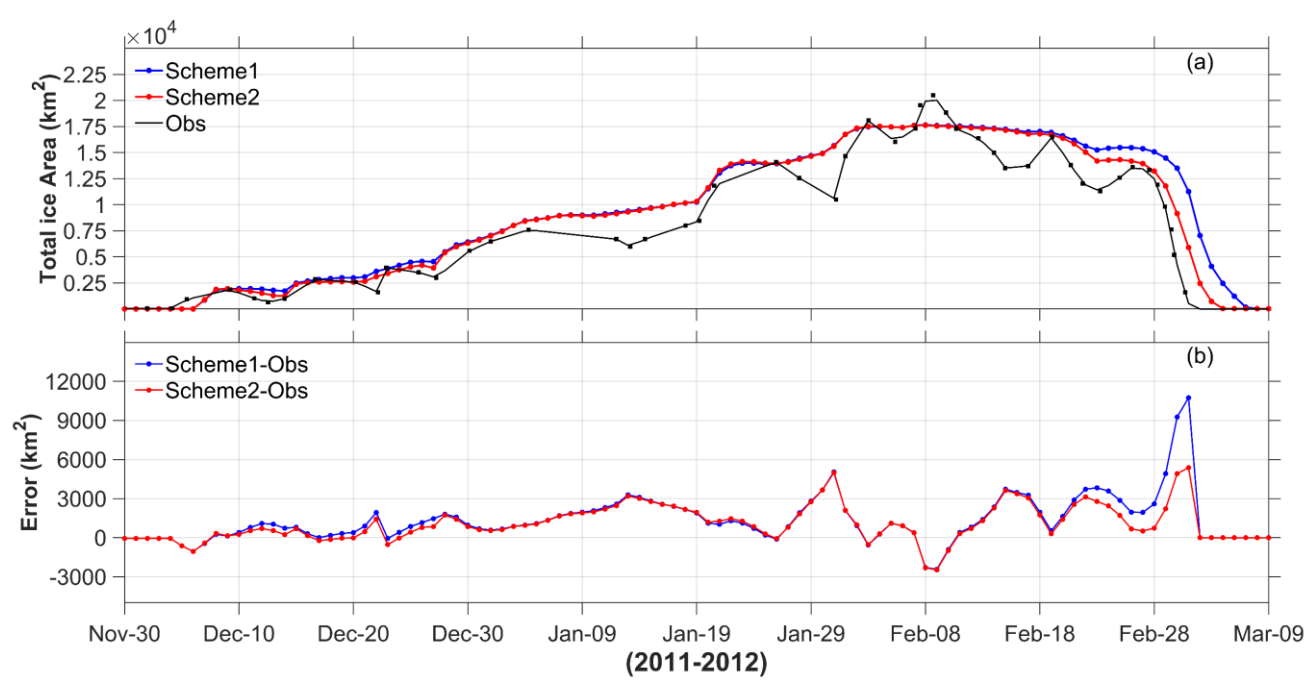


Figure 5: (a) Time series of simulated total ice area for Scheme1 (blue line), Scheme2 (red line) and that calculated from satellite observation data (black line); (b) Time series of simulated total ice area errors between Scheme1 and observations (Scheme1-Obs, blue line), and that between Scheme2 and observations (Scheme2-Obs, red line).

Table 2 presents a quantitative comparison of the maximum total ice area and ice season length simulated by the two parameterization schemes. The root mean square error (RMSE) of the total ice area simulated by the two schemes was also calculated. Both schemes underestimate the maximum total ice area by approximately 12 % (mainly during the melt period and terminal ice period, shown in Fig. 5b), suggesting shared deficiencies in their ice thermodynamic module, particularly in the treatment of ice-ocean interface heat exchange which determines the ice melting. However, Scheme2 demonstrates superior performance in the overall accuracy, as evidenced by its lower RMSE (1,446 km² versus 2,012 km² for Scheme1). This suggests that Scheme2 more reliably captures the spatial extent and temporal evolution of sea ice, despite similar peak ice area estimates. Nevertheless, Scheme2 exhibits a limitation in simulating ice season length, underestimating it by 16 days, whereas Scheme1 shows better agreement with observations (only 7-day underestimation).

Table 2. Comparison of simulated maximum total ice area, ice season length and the RMSE of total ice area for Scheme1 and Scheme2 against satellite observations in the Bohai Sea.

Metrics	Obs.	Scheme1	Scheme2	
				-



225



Maximum total ice area (km²)	20021	17645	17625
Ice season length (day)	123	116	107
RMSE of total ice area (km²)	-	2012	1446

#### 3.2.2 Ice concentration and thickness

Figure 6 compares the spatial distributions of the simulated ice concentration ( $A_i$ ) between the two parameterization schemes on the five representative days. It's found that both schemes can simulate the gradual ice expansion from formation to peak conditions, followed by retreat during melt. For the first four periods (days  $50-110\pm10$ ), the spatial patterns of the two schemes were consistent, while in the MIZ, Scheme1 consistently yields higher  $A_i$ . The most pronounced discrepancy occurs during the fifth period (day  $130\pm10$ , terminal ice period), with significant differences extending beyond the MIZ into central-eastern Liaodong Bay.

Figure 7 compares the spatial distributions of the simulated ice thickness ( $H_i$ ) between the two schemes on the five representative days. Scheme1 produces thicker ice than Scheme2, especially in the MIZ, which is consistent with the ice concentration results. These differences primarily arise from the higher ice-ocean drag coefficient ( $C_{dw}$ ) of Scheme1, which enhances vertical mixing in open water. Stronger mixing brings more oceanic heat toward the sea surface, accelerating seawater cooling and increasing freezing rates.





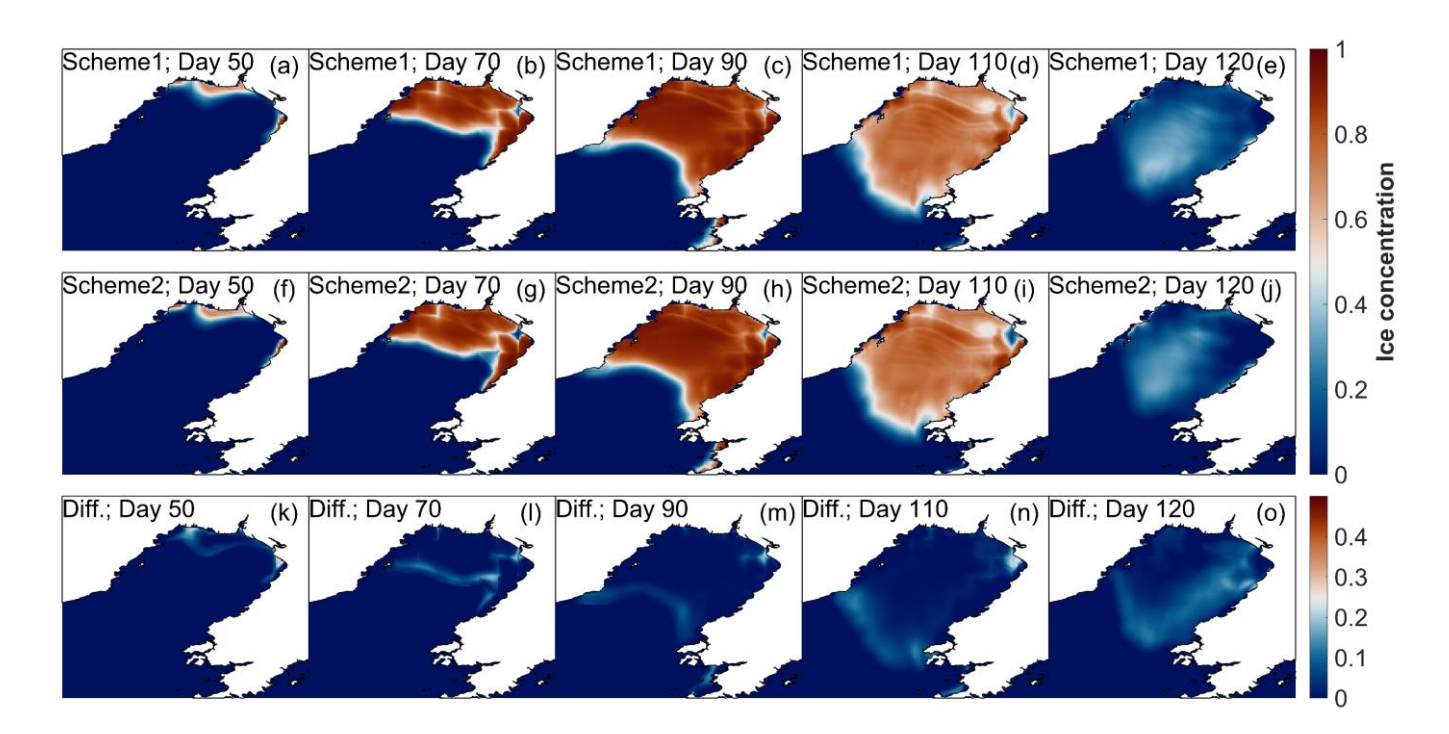


Figure 6: The simulated ice concentration distributions of Scheme1 (6(a), 6(b), 6(c), 6(d), 6(e)), Scheme2 (6(f), 6(g), 6(h), 6(i), 6(j)), and the difference between Scheme1 and Scheme2 (Scheme1-Scheme2) (6(k), 6(l), 6(n), 6(n), 6(o)) on the five representative days.

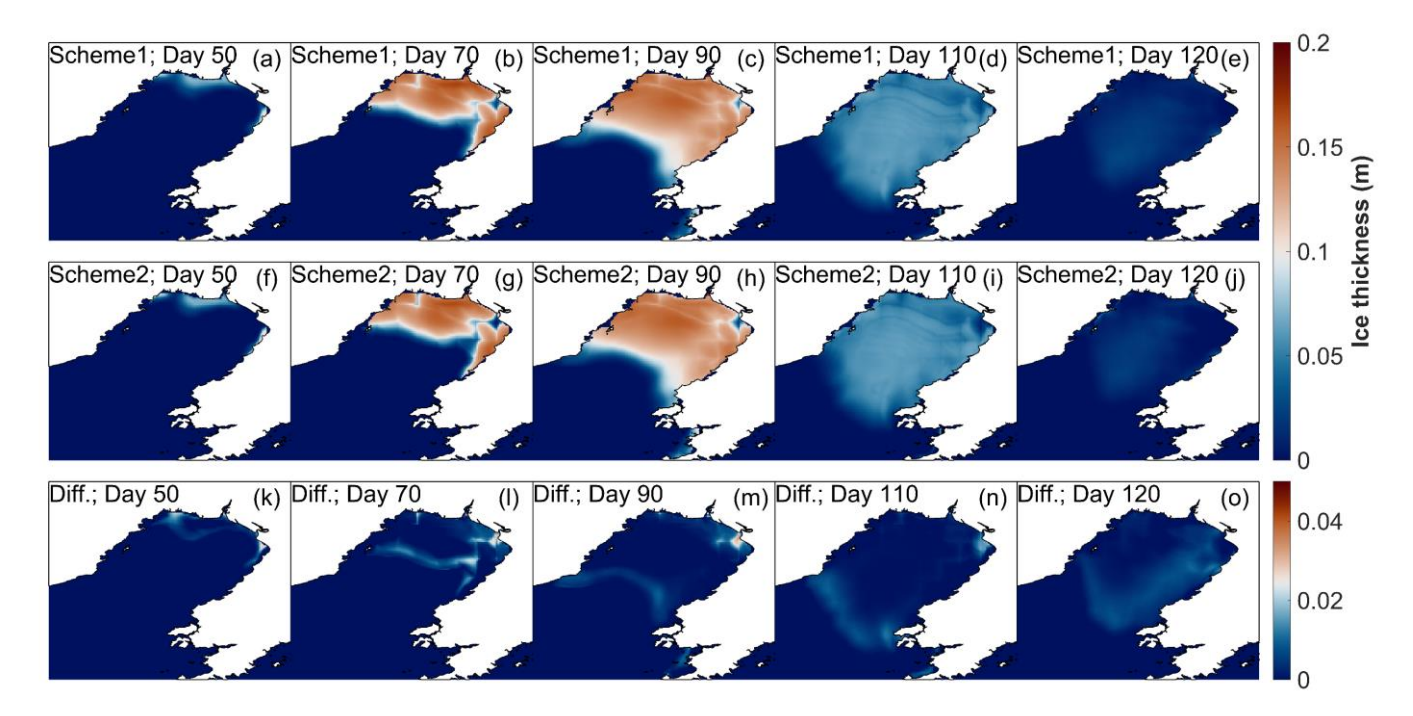






Figure 7: The simulated ice thickness distributions of Scheme1 (7(a), 7(b), 7(c), 7(d), 7(e)), Scheme2 (7(f), 7(g), 7(h), 7(j)), and the difference between Scheme1 and Scheme2 (Scheme1-Scheme2) (7(k), 7(l), 7(m), 7(n), 7(o)) on the five representative days.

#### **240 3.2.3** Ice velocity

245

250

Figure 8 presents the simulated ice velocity distributions of the two schemes on the five representative days. It can be seen that ice drifts north-eastward driven by north-westerly monsoons and surface cyclonic circulation. In Scheme1, the peak velocity occurs in the outermost edge in the MIZ, where the ice-ocean drag coefficient ( $C_{dw}$ ) drops to the lowest level across the entire ice region (approximately  $1 \times 10^{-3}$ , please see Fig. 3a to 3e). However, when  $C_{dw}$  reaches its maximum near the MIZ, the ice velocity remains at a low value. Similar situation also occurred in Scheme2, i.e., the low values of  $C_{dw}$  in the MIZ correspond to the high values of the ice velocity, and conversely, the high values of  $C_{dw}$  in the interior zone correspond to the low values of the ice velocity. When explaining this phenomenon, the ice-ocean interfacial stress  $\tau_w$  (Eq. (A1) in the appendix) is an important factor that needs to be taken into consideration. The higher drag coefficient  $C_{dw}$  results in enhanced interfacial stress  $\tau_w$ , which dissipates a larger portion of the kinetic energy input from the atmosphere, thereby restraining ice motion. In the interior ice zone, the ice velocity is also suppressed to low levels due to internal ice stress. These patterns demonstrate a synergistic negative feedback mechanism between the ice-ocean drag coefficient and internal ice stress in regulating ice motion: an increase in the drag coefficient  $\rightarrow$  enhanced ice-ocean interfacial stress  $\rightarrow$  greater dissipation of kinetic energy  $\rightarrow$  deceleration of sea ice.

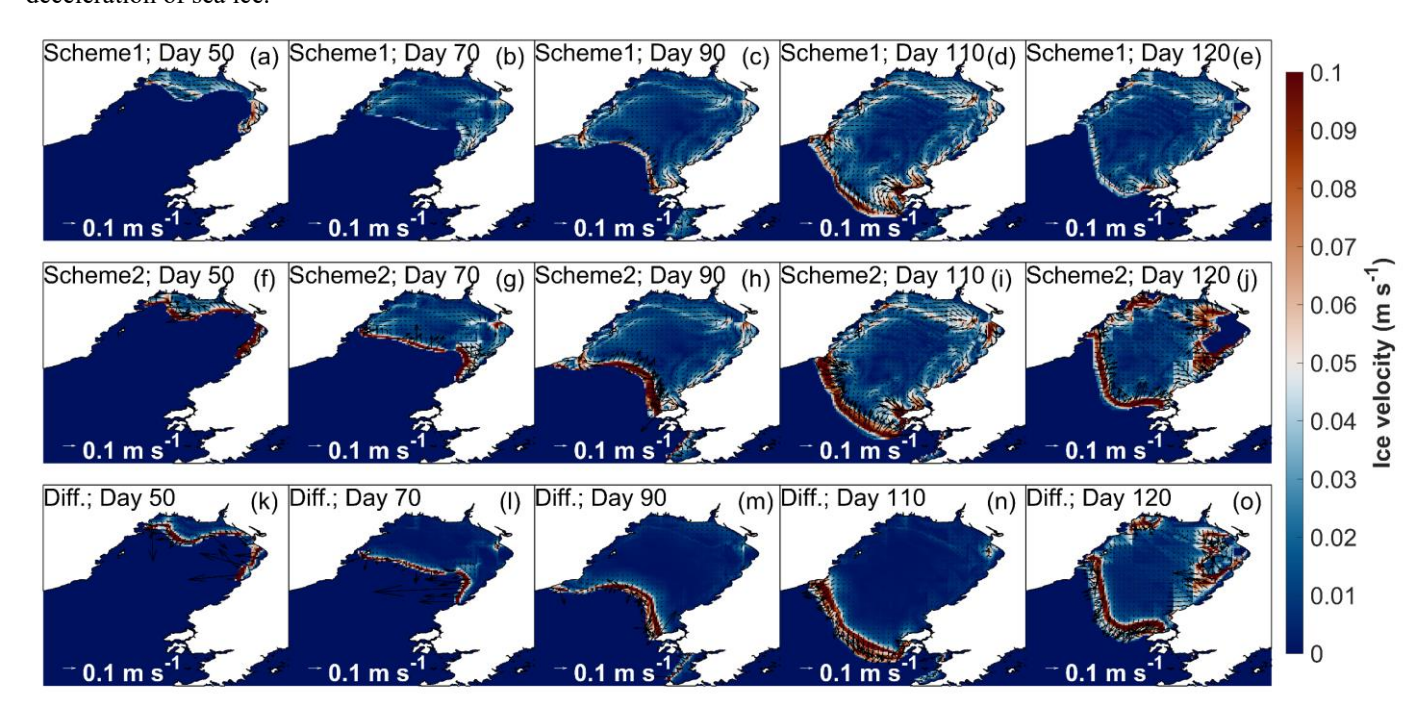


Figure 8: Vector distributions of sea ice velocity of Scheme1 (8(a), 8(b), 8(c), 8(d), 8(e)) and Scheme2 (8(f), 8(g), 8(h), 8(i), 8(j)), and the difference between Scheme1 and Scheme2 (Scheme1-Scheme2) (8(k), 8(l), 8(m), 8(n), 8(o)) on the five representative days.



265

270



#### 3.3 Impact on ice-ocean interface variables

Through the analysis of the spatiotemporal distributions and variations of the ice-ocean drag coefficient and sea ice variables, we found that Scheme1 consistently simulates higher ice concentration and thickness, especially in the MIZ. The differences between the two schemes become significantly more pronounced after the melt period (post-day 110). Previous studies have shown that the sea ice freezing/melting evolution in the Bohai sea is mainly controlled by its thermodynamic processes (Wang et al., 2000; Wang et al., 1984). In view of this, in addition to the  $C_{dw}$  dynamic regulation mechanism in section 3.2.3, the thermodynamic regulation mechanism is also worth exploring. Therefore, in order to conduct a more comprehensive investigation into the differences in sea ice variables resulting from the two schemes, the thermodynamic variables at the ice-ocean interface are analyzed in this section to reveal the  $C_{dw}$  thermodynamic regulation mechanism.

The model's predefined grid area contains sea ice with an ice concentration of  $A_i$  (including both pre-existing and newly formed sea ice), while the remaining  $1 - A_i$  area consists of open water (shown in Fig. 9). At the ice-ocean interface, the heat flux variation balances the latent heat sink or source caused by melting or freezing. The heat flux  $Q_{oi}$  transported from the mixed layer to the sea ice base drives the phase change process at the bottom of the sea ice: a portion of the heat  $(Q_l)$  is absorbed as latent heat of phase transition, while the remaining heat  $(Q_c)$  is conducted into the interior of the sea ice, Here,  $Q_l = Q_{oi} - Q_c$  (Holland and Jenkins, 1999).

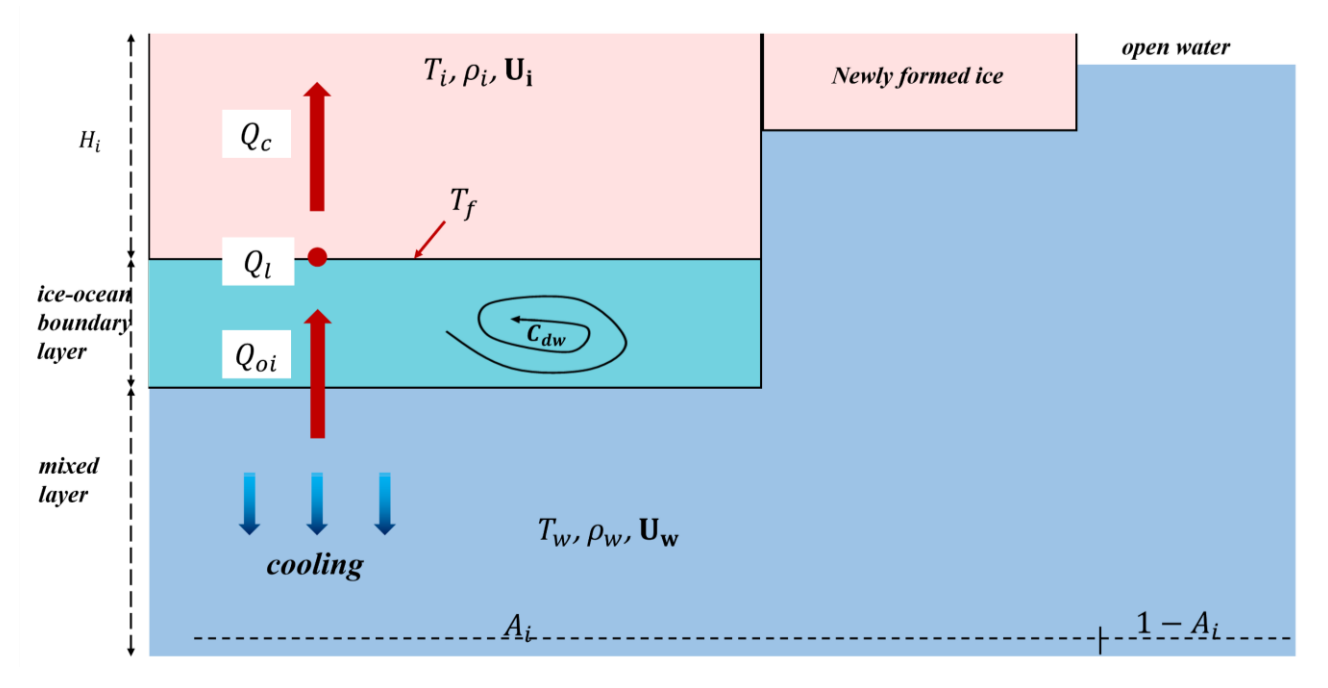


Figure 9: Schematic diagram of thermodynamic and dynamic processes at the ice-ocean interface. Within the grid cell, sea ice concentration  $A_i$  (representing existing ice and newly formed ice), along with ice variables (ice temperature  $T_i$ , ice density  $\rho_i$ , ice velocity  $U_i$ , freezing point temperature  $T_f$ ) and mixed layer variables (water temperature  $T_w$ , water density  $\rho_w$ , current velocity  $U_w$ ) are shown. The diagram depicts heat flux pathways:  $Q_{oi}$  represents heat flux transfer from the mixed layer to the ice base;  $Q_c$ 



280

285

295

300

305



represents the conductive heat flux within the sea ice interior; and  $Q_l$  represents the latent heat absorbed or released during phase change at the ice base.

The temporal evolution of the key ice-ocean thermodynamic variables averaged over ice-covered areas for Scheme1 and Scheme2 is shown in Fig. 10, while the differences between the two schemes (Scheme1 – Scheme2) are also quantified in Fig. 11. As shown in Fig. 10a and Fig. 11a, the ice-ocean drag coefficient  $C_{dw}$  exhibits distinct behaviors between schemes. Scheme1 maintains higher and relatively stable  $C_{dw}$  values, decreasing gradually to a minimum of  $0.8 \times 10^{-3}$  by the terminal ice period. In contrast, Scheme2 shows a smoother temporal variation, with  $C_{dw}$  increasing from initial ice period, peaking during the peak ice period (though still lower than Scheme1), and declining thereafter. This discrepancy directly modulates momentum and heat exchange at the ice-ocean interface, leading to subsequent differences in heat and momentum flux between the two schemes across the ice-ocean boundary. Figure 10b displays the oceanic heat flux  $Q_{oi}$ , calculated using the bulk formula proposed by Mcphee (1992):

$$Q_{oi} = \rho_w c_{pw} \Delta T C_h u_* \,, \tag{1}$$

where  $\rho_w$  is seawater density,  $c_{pw}$  is specific heat capacity,  $\Delta T = T_f - T_w$  is the temperature difference between the freezing point and mixed layer temperature,  $C_h$  is the interfacial heat transfer coefficient, and the friction velocity  $u_*$ , which calculated by  $C_{dw}$  and the velocity difference between ice and ocean, describes the intensity of turbulent momentum exchange at the ice-ocean interface (Mcphee, 2017):

$$u_* = \sqrt{C_{dw}} |U_w - U_i|, \qquad (2)$$

Due to its higher  $C_{dw}$ , Scheme1 generates significantly greater  $u_*$  and  $Q_{oi}$  than Scheme2, particularly during the terminal ice period (see Fig. 11b). Figures 10c to 10d compare the ice base variation rate  $R_b$  and newly formed ice growth rate  $R_{new}$ , their differences between the two schemes are shown in Fig. 11c to 11d. And Fig. 10f to 10g present the mixed layer temperature reduce due to the heat loss to sea ice ( $\Delta T_{oi}$ ) and the supercooling temperature when seawater drops to the freezing point ( $\Delta T_{sc}$ ), their differences between the two schemes are also shown in Fig. 11f to 11g. It's found that the enhanced  $Q_{oi}$  in Scheme1 drives markedly higher basal melt rates compared to Scheme2. Paradoxically, Scheme1 also exhibits a greater new ice production for most of the simulation, with a minor peak during the terminal ice period. This dual effect likely stems from the competing roles of  $C_{dw}$ : while higher  $C_{dw}$  intensifies basal melt ( $R_b$ ) via increased  $Q_{oi}$ , it also strengthens vertical mixing, accelerating heat dissipation from the mixed layer ( $\Delta T_{oi}$ ) and promoting supercooled water formation ( $\Delta T_{sc}$ ), thereby enhancing the newly formed ice ( $R_{new}$ ). Figure 10e shows the weighted total ice base variation rate ( $R_{tol} = A_i \cdot R_b + (1 - A_i) \cdot R_{new}$ ), which reflects the net ice base variation. Notably, the  $R_{tol}$  difference in Fig. 11e peaks between December 19-29, 2012, aligning with concurrent disparities in ice concentration (Fig. 11h) and ice thickness (Fig. 11i).





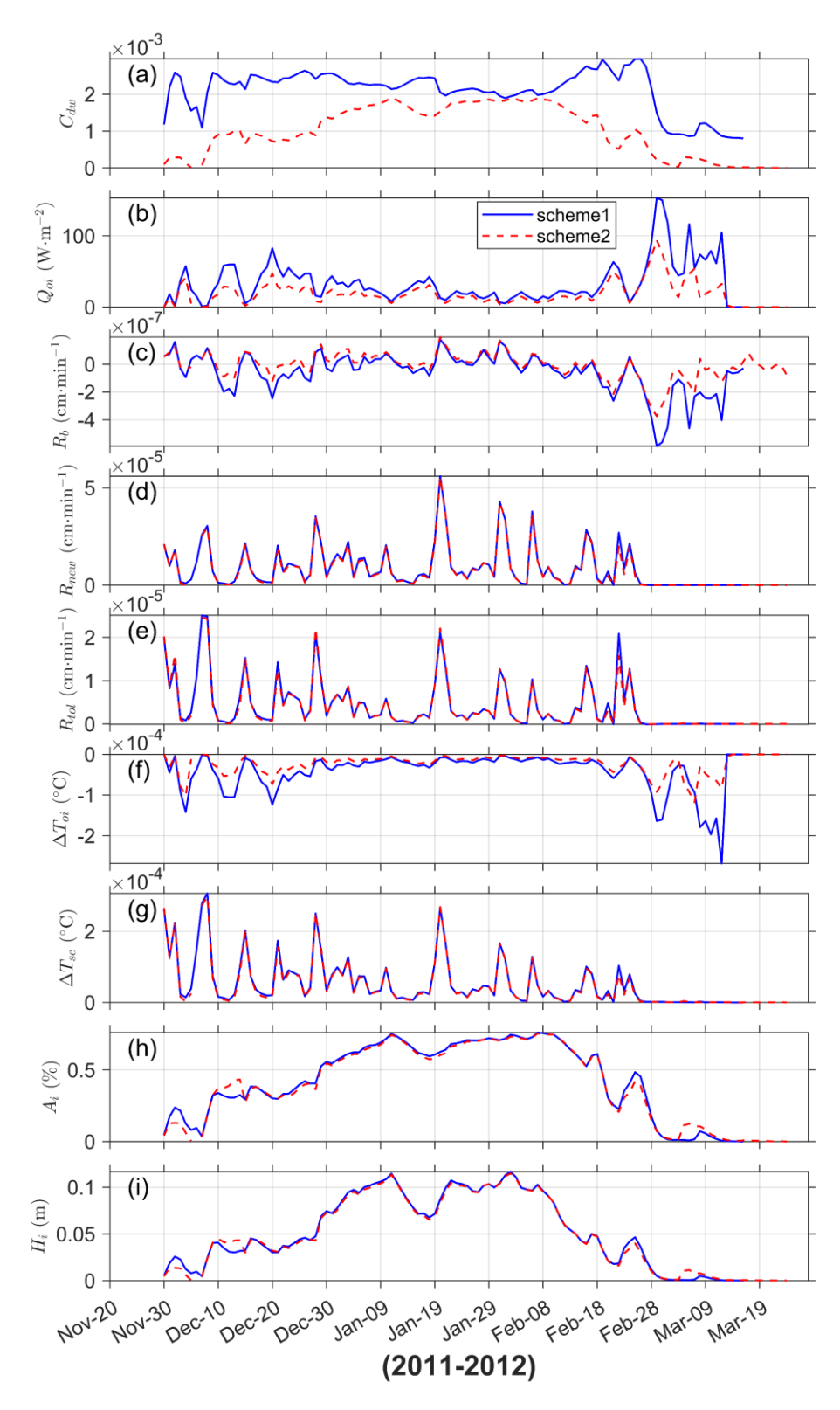


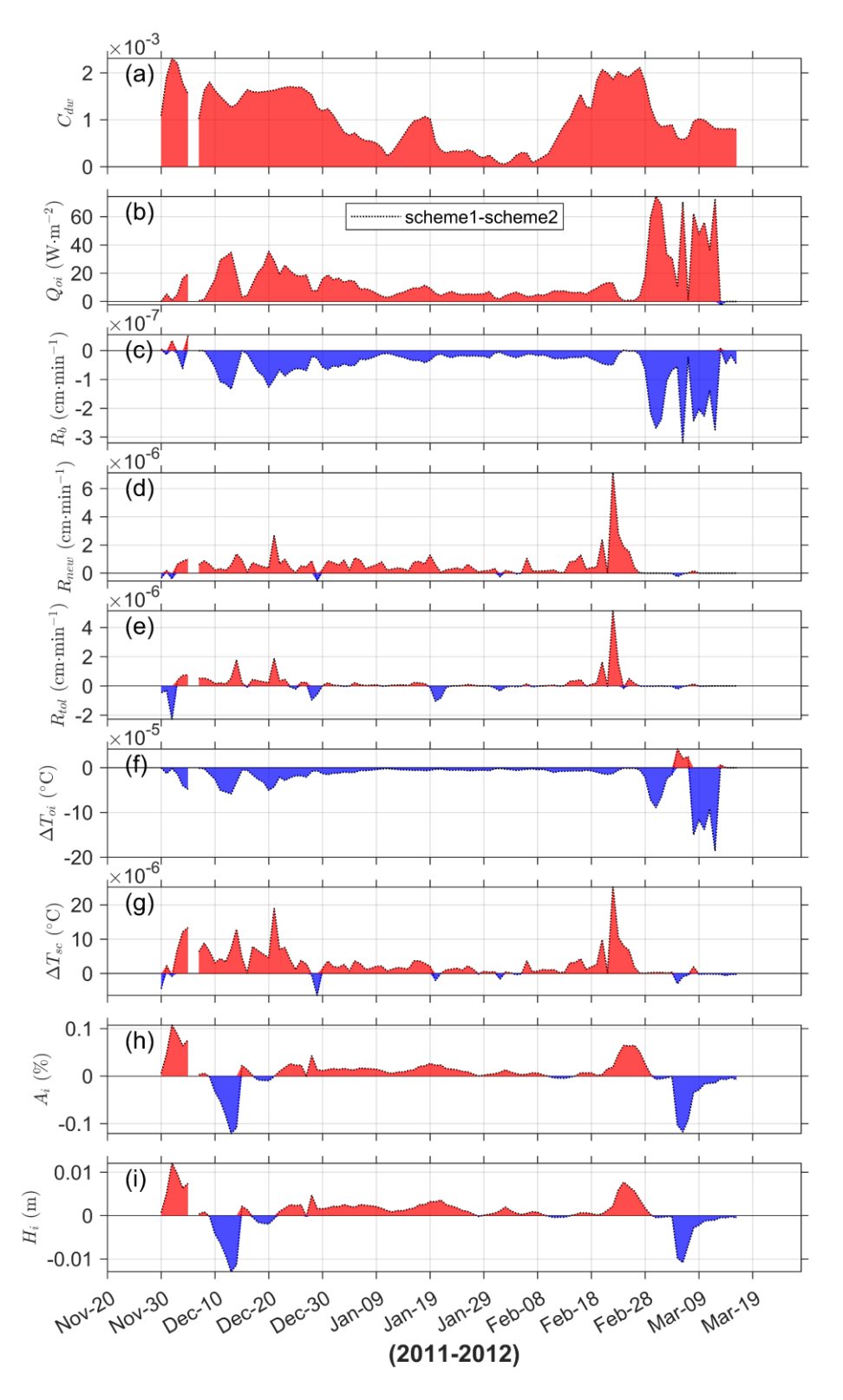




Figure 10: The time series of the region-averaged values of the ice-covered areas in the ice-ocean interface variables, ice-ocean drag coefficient  $C_{dw}$  (a), oceanic heat flux  $Q_{oi}$  (b), ice base variation rate  $R_b$  (c), newly formed ice growth rate  $R_{new}$  (d), the sum of the weighted values of the newly formed ice growth rate and the ice base variation rate  $R_{tol}$  (e), the mixed layer temperature reduce due to the heat loss to sea ice  $\Delta T_{oi}$  (f), supercooling temperature when seawater drops to the freezing point  $\Delta T_{sc}$  (g), ice concentration  $A_i$ (h), and ice thickness  $H_i$  (i). The positive value for (c), (d), and (e) represents the freezing rate, and negative value represents the melting rate.









325



Figure 11: Time series of the differences (Scheme1 - Scheme2) of the ice-ocean interface variables: ice-ocean drag coefficient  $C_{dw}$  (a), oceanic heat flux,  $Q_{oi}$  (b), ice base variation rate  $R_b$  (c), newly formed ice growth rate  $R_{new}$  (d), the sum of the weighted values of the newly formed ice growth rate and the ice base variation rate  $R_{tol}$  (e), the mixed layer temperature reduce due to the heat loss to sea ice  $\Delta T_{oi}$  (f), supercooling temperature when seawater drops to the freezing point  $\Delta T_{sc}$  (g), ice concentration  $A_l$  (h), ice thickness  $H_l$  (i).

Finally, the ice concentration (Fig. 10h) and thickness (Fig. 10i) are directly governed by the total ice variation rate. This indicates that the variation of the drag coefficient has a double thermodynamic influence on the ice variables at the ice-ocean interface: they regulate basal melt via  $Q_{oi}$ , while simultaneously stimulating new ice formation through mixed-layer cooling, with their net effect dictating total ice evolution. Despite the elevated basal melt rates  $R_b$  of Scheme 1, newly formed ice growth rate  $R_{new}$  ultimately dominate, leading to lower net ice loss, especially during the terminal ice period. Therefore, by evaluating a series of responses of the thermodynamic variables at the ice-ocean interface to variations in the two drag coefficient parameterization schemes, it can be determined that  $C_{dw}$  regulates sea ice formation and melt through both positive and negative feedback mechanisms (please see Fig. 12).

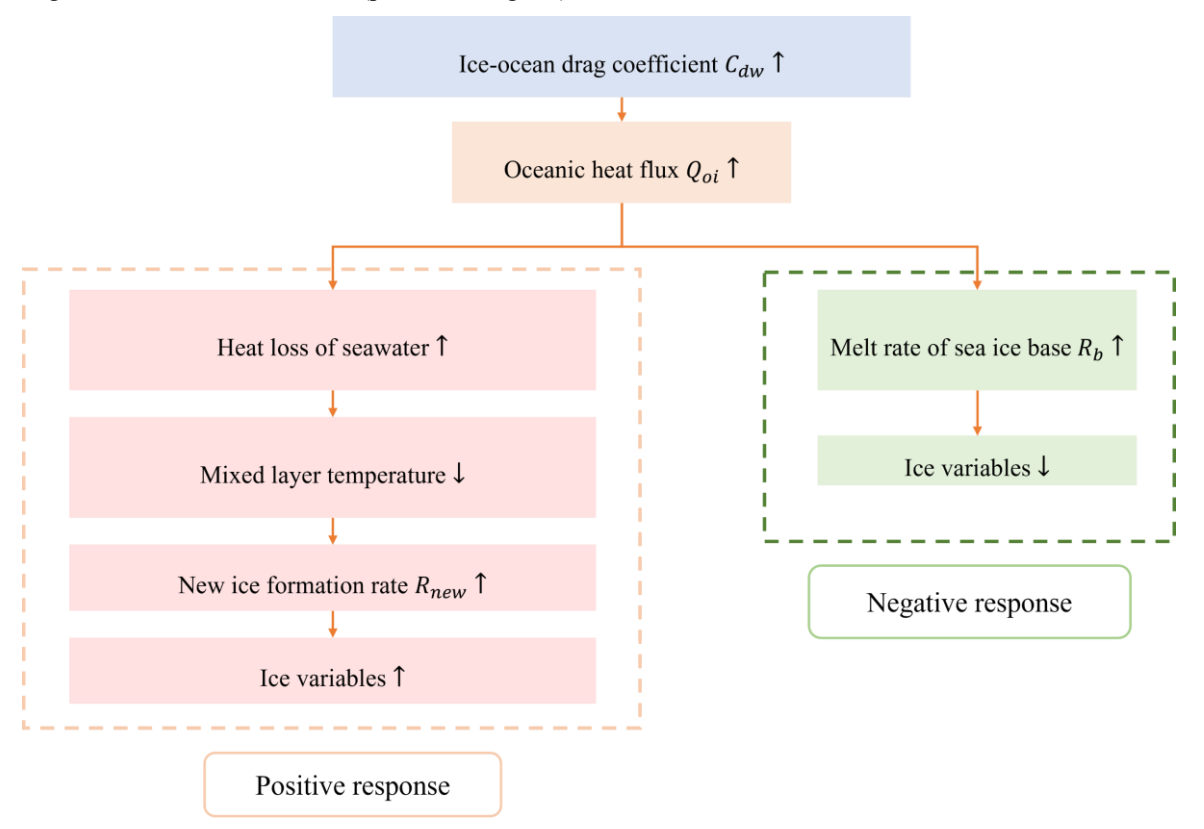


Figure 12: Schematic diagram of the dual impact mechanisms of the ice-ocean drag coefficient on sea ice variables.





#### 4 Conclusion

335

340

345

350

This study systematically compares two ice-ocean drag coefficient parameterization schemes: a large-scale roughness-based parameterization (Scheme1) and a small-scale geometric roughness-based parameterization (Scheme2), in simulating Bohai Sea ice evolution. The findings reveal the dynamic and thermodynamic mechanisms in how the ice-ocean drag coefficient  $(C_{dw})$  controls sea ice variables, and highlight the distinct performances of the two schemes.

Scheme1 considers the relationship between the large-scale sea ice roughness elements (deformation energy (R) and ice concentration  $(A_i)$ ) and the ice-ocean drag coefficient, resulting in higher  $C_{dw}$  values, particularly in the MIZ. This enhances ice-ocean momentum mixing, prolonging ice retention and improving the simulation of ice season length (underestimating by only 7 days compared to 16 days in Scheme2). In contrast, Scheme2 partitions  $C_{dw}$  into skin drag  $(C_{dw}^s)$ , form drag from keels  $(C_{dw}^r)$ , and form drag from floe edges  $(C_{dw}^f)$ . The simulated partial drag coefficients indicate that skin drag dominates, accounting for approximately 80 % of the total ice-ocean drag. Scheme2 improves the overall spatial and temporal evolution of sea ice (reducing the RMSE of total ice area by 28 % compared with Scheme1) and yields faster ice drift in the MIZ, as lower  $C_{dw}$  reduces oceanic drag, allowing atmospheric forcing to dominate.

Dynamically, ice velocity is significantly affected by the ice—ocean drag coefficient  $C_{dw}$ . A negative feedback mechanism was discovered in the regulation of ice motion by  $C_{dw}$ : an increase in the  $C_{dw} \rightarrow$  enhanced ice—ocean interfacial stress  $\rightarrow$  greater dissipation of kinetic energy  $\rightarrow$  deceleration of sea ice. Thermodynamically, Scheme1 produces larger ice area, ice concentration and thickness compared to Scheme2, particularly after the melt period. These differences arise from dual thermodynamic feedbacks mediated by  $C_{dw}$ . A higher  $C_{dw}$  increases the oceanic heat flux to the ice base, accelerating basal melting, but also strengthens vertical mixing, which cools the mixed layer and promotes new ice formation in open-water areas. Future work can focus on hybridizing the schemes to leverage their respective strengths, refining the relationship of  $C_{dw}$  and the ice-ocean dynamic and thermodynamic processes for shallow seas. These advancements will enhance regional sea-ice forecasting and clarify drag-mediated feedbacks in a changing climate.





#### Appendix A

360

365

370

In the sea ice numerical simulations, the tangential stress  $\tau_w$  from the ocean, also known as the ice-ocean surface drag, is commonly described using the quadratic bulk formula (Mcphee, 1979):

355 
$$\tau_{w} = \rho_{w} c_{dw} |\mathbf{U}_{w} - \mathbf{U}_{i}| \begin{bmatrix} \cos \theta & -\sin \theta \\ \sin \theta & \cos \theta \end{bmatrix} (\mathbf{U}_{w} - \mathbf{U}_{i}), \qquad (A1)$$

where  $\rho_w$  represents the density of sea water,  $U_w$  is the drift velocity of ocean current,  $U_i$  is the ice-drift velocity.  $\theta$  is the rotation angle of ocean induced by the Coriolis force. The ice-ocean drag coefficient  $C_{dw}$  is a key parameter that describes the efficiency of horizontal momentum exchange between sea ice and the ocean, and is closely related to sea ice surface roughness. The two parameterization schemes of  $C_{dw}$  applied in this study, which utilize representations of sea ice roughness at different spatial scales, will be described in detail below.

## 1 Scheme1: Large-scale roughness-based parameterization

In the original ice-ocean drag coefficient parameterization scheme of the model, the magnitude of the ice-ocean drag coefficient is mainly determined by the bottom surface roughness of sea ice. The parameterization scheme using deformation energy R to characterize large-scale sea ice roughness was first proposed by Steiner et al. (1999). Here, the deformation energy R reflects the accumulation of deformation of sea-ice by internal forces. In this scheme, the ice-ocean drag coefficient  $C_{dw}$  is parameterized as a function of the deformation energy R and the ice concentration  $A_i$ :

$$C_{dw} = m_w R + b_w - 4d_w \left( A_i - \frac{1}{2} \right)^2 + d_w , \qquad (A2)$$

where  $b_w$  is the ice-ocean interfacial skin drag constant, which represents the skin drag portion. Except for  $b_w$ , all the terms on the right side of the equal sign collectively represent the form drag portion.  $m_w$  and  $d_w$  are the form drag constants. The deformation energy R is introduced as a scalar ice property variable governed by dynamic and thermodynamic processes. For a detailed derivation, please refer to Steiner et al. (1999). Here,  $A_i$  represents ice concentration. The setting values of the constant parameters in Scheme1 are shown in Table A1.

Table A1. The model parameter settings of Scheme1.

Parameterization Scheme1		
$m_w$	$4.0 \times 10^{-8}$	
$b_w$	$1.2 \times 10^{-3}$	
$d_w$	$2.6 \times 10^{-3}$	

# 5 2 Scheme2: Small-scale geometric roughness-based parameterization

Different to the original scheme of the model (Scheme1), Scheme2 involves the geometric elements generated by the deformation of sea ice within the grid with the ice-ocean drag coefficient. Here, the small-scale geometric roughness elements



385

390

395



refer to the geometric elements for ice pressure ridges (specifically ice keels). Ice pressure ridge is a bulge formed by the accumulation of debris produced by the compression of sea ice, including the sails (the above-water portions) and keels (the submerged portions). Observational studies have demonstrated that while ice pressure ridge morphology and dimensions lack standardized shapes or sizes (Rothrock and Thorndike, 1980; Timco and Burden, 1997), all observed pressure ridges exhibit significantly greater longitudinal extension compared to their transverse dimensions.

Based on existing descriptions of ice pressure ridge profiles (Davis and Wadhams, 1995; Steiner et al., 1999; Kovacs, 1970; Tsamados et al., 2014), we propose a simplified idealized ice floe model (see Fig. A1). Assuming a grid with a transverse length of  $L_x$ , longitudinal length of  $L_y$ , and the total area of the grid  $(S_T)$  contains an idealized floating ice model with N ridges distributed linearly along the longitudinal direction. Each ice ridge has a length of  $L_y$ , with an average ice floe length (x-direction) of L ( $L \ll L_x$ ) and an average ice floe spacing of  $D_f$ . The true ice thickness is defined as  $D_{ice} = H_i / A_i$ , where  $H_i$  is grid-averaged ice thickness and  $A_i$  is the ice concentration. Here, the freeboard height and draft depth are denoted as  $h_f$  and  $h_d$ , respectively. The overall height of the ice ridge is the sum of  $h_{sm}$  for sail and  $h_{km}$  for keel, with grid-averaged vertical spacings of  $D_{sm}$  between adjacent sails and  $D_{km}$  between adjacent keels. Unlike multiyear ice, which typically exhibits a Gaussian-shaped cross-section, first-year ice ridges tend to have triangular profiles at both the sail and keel tops.

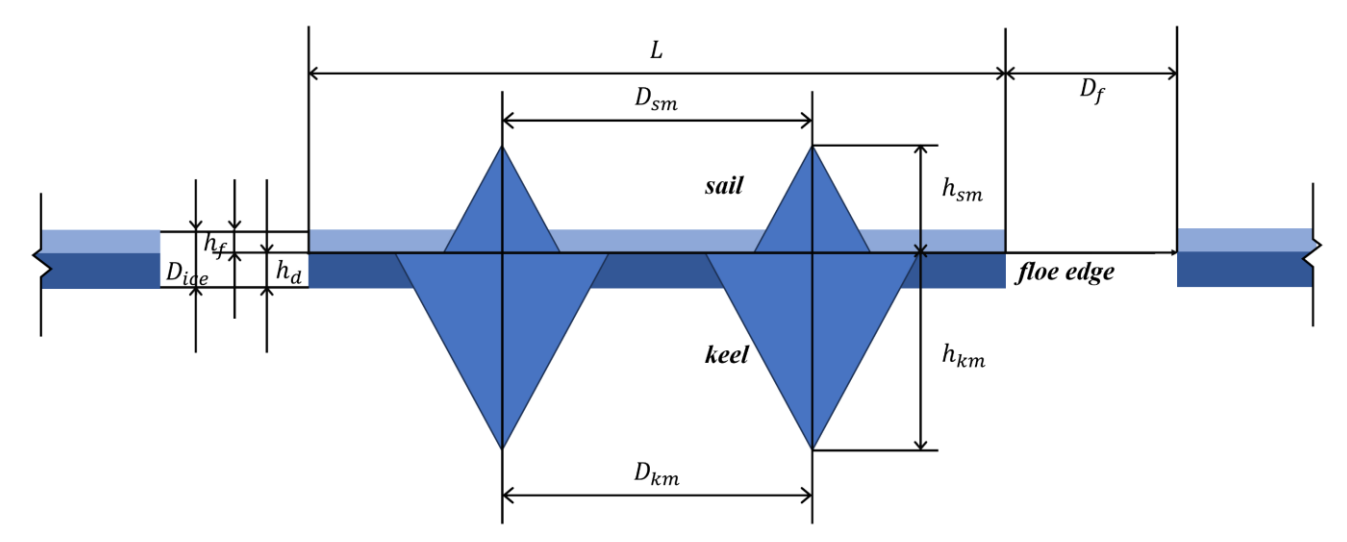


Figure A1: The idealized ice floe model features an ice floe with a length of L and a spacing of  $D_f$ . The above-water portions of the ice ridges, referred to as sails, have an average spacing of  $D_{sm}$  and an average height of  $h_{sm}$ . Correspondingly, the submerged portions, known as keels, exhibit an average spacing of  $D_{km}$  and an average height of  $h_{km}$ . The true ice thickness  $D_{ice}$  includes the freeboard height  $h_f$  and the draft depth  $h_d$ .

# 2.1 General form of the ice-ocean drag coefficient $C_{dw}$

In this parameterization scheme, the general form of the ice-ocean drag coefficient  $C_{dw}$  was derived by Tsamados et al. (2014):

$$C_{dw} = \frac{NcS_c^2 g L_y H}{2S_T} \left[ \frac{\ln(H/z_0)}{\ln(10/z_0)} \right]^2, \tag{A3}$$





- where N represents the number of obstacles with longitudinal length  $L_y$  within a grid of area  $S_T$ , c is the drag constant which account for drag on individual elements. H is the obstacle height, and  $z_0$  is the roughness length. g denotes a geometric factor dependent on obstacle shape. For uniformly distributed linear obstacles (e.g., ice ridges or floe edges), the geometric factor g can be obtained through directional averaging of the angle  $\theta$  between the obstacle normal and flow direction, expressed as  $g = \int_{-\frac{\pi}{2}}^{\frac{\pi}{2}} \frac{1}{\pi} cos\theta d\theta$ .
- Here,  $S_c$  is the sheltering function. The sheltering effect has significant physical implications as it describes how upstream obstacles (e.g., ice ridges or floes) modify water flow by creating drag and subsequent turbulent wakes. This wake effect reduces the current velocity experienced by downstream obstacles, thereby effectively decreasing downstream drag (Arya, 1975; Steele et al., 1989). In MIZ where ice ridges and floes exhibit irregular geometries, drag arises not only from skin friction but also from form drag (Tsamados et al., 2014). Under such conditions, the sheltering effect becomes particularly pronounced.
- 410 For modelling purposes, Tsamados et al. (2014) employed a sheltering function  $S_c$ :

$$S_c = \left[1 - \exp\left(-s_l \frac{D}{H}\right)\right]^{1/2},\tag{A4}$$

Here,  $s_l$  is the attenuation parameter, D represents the distance between obstacles, and H denotes obstacle height. Research indicates that the sheltering effect parameter  $s_l$  exhibits significant variation depending on medium conditions. In this study, we adopt the configuration of Tsamados et al. (2014), employing the value  $s_l = 0.18$  proposed by Hanssen-Bauer and Gjessing (1988).

#### 2.2 Total ice-ocean drag coefficient

415

According to the drag partitioning theory of Arya (1975), the interfacial drag between sea ice and fluid (sea water) can be decomposed into form drag induced by obstacles (e.g., ice floes/ridges) and skin drag arising from tangential shear in the intervening areas. The form drag contribution from ice floe edges, first parameterized by Hanssen-Bauer and Gjessing (1988),

420 allows the total drag coefficient  $C_{dw}$  to be expressed as:

$$C_{dw} = C_{dw}^r + C_{dw}^s + C_{dw}^f , \tag{A5}$$

where  $C_{dw}$  is the total drag coefficient,  $C_{dw}^r$  is form drag coefficient related to obstacles,  $C_{dw}^s$  is skin drag coefficient, and  $C_{dw}^f$  is the form drag related to ice floe edge.

# 2.2.1 Form drag coefficient $C_{dw}^r$

Building upon the ice ridge parameterization scheme of Tsamados et al. (2014), the relationship for total ridge length per unit ice area  $\frac{NL_y}{A_iS_T}$  in Eq. (A4) is given by  $\frac{NL_y}{A_iS_T} = \frac{\pi\mu}{2}$ , where  $\mu = \frac{1}{D}$  represents the number of ridges per unit track length, with D being the ridge spacing. By incorporating the small-scale geometric roughness elements (average height of ice keel  $h_{km}$  and average spacing of ice keel  $D_{km}$ ), the expression for the ridge keel drag coefficient (i.e., the form drag coefficient)  $C_{dw}^r$  can be obtained as:





430 
$$C_{dw}^r = \frac{1}{2} c_{kw} S_c^2 \frac{h_{km}}{D_{km}} A_i \left[ \frac{\ln(h_{km}/Z_{0i})}{\ln(10/Z_{0i})} \right],$$
 (A6)

where  $A_i$  is the sea ice concentration,  $c_{kw} = 0.2$  denotes the local form drag constant, and  $z_{0i}$  represents the roughness length of level ice.

# 2.2.2 Skin drag coefficient $C_{dw}^{s}$

Based on the parameterization scheme of Arya (1975), the ice-ocean interfacial skin drag coefficient can be expressed as:

435 
$$C_{dw}^{s} = A_{i} \left( 1 - m_{w} \frac{h_{km}}{D_{km}} \right) c_{sw}, \text{ if } \frac{h_{km}}{D_{km}} \le \frac{1}{m_{w}},$$
 (A7)

where  $m_w$  is a parameter related to keel height but typically assumed constant (here  $m_w = 10$ ), and  $c_{\rm sw}$  represents the unobstructed surface skin drag coefficient, which is attained in the absence of keels and under complete ice cover ( $A_i = 1$ ). We adopt the default value  $c_{\rm sw} = 0.002$ .

## 2.2.3 Calculation of the grid-averaged height of ice keel $h_{km}$

The grid-averaged height of ice keel  $h_{km}$  is a key variable in the equations of form drag coefficient  $C_{dw}^s$  and skin drag coefficient  $C_{dw}^s$ . Here, we adopt the scheme first proposed by Steiner et al. (1999) which derives  $h_{km}$  by examining the transfer of deformation energy into potential energy within ridges during ice ridging. The relationship between the potential energy P transferred into ridges and the total deformation energy R is expressed as a fractional ratio (Rothrock, 1975):

$$P = C_R \cdot R \,, \tag{A8}$$

Here,  $C_R$  is a scaling factor. Following Steiner et al. (1999),  $C_R$  is set as 7.5 %. To determine  $h_{km}$ , the potential energy  $P_k(h_k)$  corresponding to the keel height  $h_k$  must be calculated as follows:

$$P_k(h_k) = \Delta \rho g(c_1 h_k^3 - c_2 D_{ice} h_k^2) , \tag{A9}$$

where  $\Delta \rho = \rho_w - \rho_i$  represents the density difference between water ( $\rho_w = 1025 \text{ kg m}^{-3}$ ) and ice ( $\rho_i = 915 \text{ kg m}^{-3}$ ),  $D_{ice} = h_d + h_f$  denotes the average true ice thickness, and  $c_1 = 0.318$ ,  $c_2 = 0.373$  are dimensionless coefficients derived

450 from Gaussian integral-based volume fraction calculations.

Observational data indicate that keel height frequencies exhibit characteristics consistent with an exponential distribution (Davis and Wadhams, 1995; Hibler Iii et al., 1972; Mock et al., 1972). Consequently, the frequency distribution  $N(h_k)$  of ridges per kilometer track satisfies:

$$N(h_k) = n_R \frac{1}{h_{km} - h_0} \exp\left(\frac{h_0 - h_k}{h_{km} - h_0}\right),\tag{A10}$$

 $N(h_k)$  describes the frequency of keels with varying draft depths  $h_k$  per unit track length. Here,  $h_0$  denotes the minimum truncation depth for keels, taken as  $h_0 = h_d + 0.75$ , with  $h_d$  being the ice draft depth. The parameter  $n_R$  indicates the frequency of keels per kilometer of track:

$$n_R = \frac{1}{c_n} \left(\frac{R}{h}\right)^q \,, \tag{A11}$$





where q is an exponent ranging between 0 < q < 1. The model adopts  $q = \frac{1}{2}$ . The parameter  $c_n$  represents an empirical constant, which is taken as  $c_n = 14 \times 10^3 \text{ J}^{1/2} \text{ m}^{-1/2}$  in the current study. h is the ice volume per area,  $h = D_{ice}/A_i$ . The total potential energy P accumulated in the keel can be obtained by integrating in the height range of the keel:

$$P = \int_{h_0}^{+\infty} P_k(h_k) N(h_k) \ dh_k \ , \tag{A12}$$

The left-hand side of the equation can be obtained from Eq. (A7), while the right-hand side is derived from Eq. (A8), Eq. (A9), and Eq. (A10). The balance equation between the potential energy P computed from deformation energy R and the potential energy stored across different keel height categories can be expressed as:

$$C_R \cdot R = \int_{h_0}^{+\infty} P_k(h_k) N(h_k) \ dh_k \,,$$
 (A13)

By solving this expression, the grid-averaged keel height  $h_{km}$  can be obtained.

# 2.2.4 Form drag coefficient of ice edge $C_{dw}^f$

Considering the geometric features of the edge of the ice floe, distance D is replaced by the typical distance  $D_f$  between the ice floe, and the obstacle height H corresponds to the submerged draft depth  $h_d$ . The normalized ice-covered area  $A_i$  can be expressed as  $A_i = \frac{Nc_{sf}L^2}{S_T}$ , where L is the average ice floe length (x-direction), and  $c_{sf}$  is a geometric parameter (taking  $\frac{\pi}{4}$  for circular ice floes or 1 for square ice floes). The total ice floe edge length per unit area then simplifies to  $\frac{NL}{S_T} = \frac{A_i}{c_{sf}L}$ . the drag coefficient for ice floe edges can be derived as:

$$C_{dw}^{f} = \frac{1}{2} \frac{c_{fw}}{c_{sf}} S_c^2 \frac{h_d}{L} A_i \left( \frac{\ln(h_d/z_{0w})}{\ln(10/z_{0w})} \right)^2, \tag{A14}$$

where  $c_{fw}$  is a constant-form local form drag coefficient, submerged draft depth is simplified as  $h_d = 0.9D_{ice}$  and  $z_{0w} = 3.27 \times 10^{-4}$  m denotes the seawater upstream roughness length of floe. Based on aerial observations from the Fram Strait (Hartmann et al., 1992), ice floe length L and spacing  $D_f$  can be parameterized as Lüpkes et al. (2012):

$$L = L_{\min} \left( \frac{A_{i_{\star}}}{A_{i_{\star}} - Ai} \right)^{\beta} , \tag{A15}$$

In the equation,  $A_{i_{\star}} = 1/[1 - (L_{\min}/L_{\max})^{1/\beta}]$  serves as a regularization parameter to eliminate the singularity at  $A_i = 1$ . For ice floe spacing, Lüpkes and Birnbaum (2005) derived based on a periodic distribution assumption:

$$D_f = L(1 - \sqrt{A_i})/\sqrt{A_i}, \qquad (A16)$$

The setting values of the constant parameters in Scheme2 are shown in Table A2.

Table A2. The model parameter settings of Scheme2.

Parameterization Scheme2			
$z_{0i}$	$5.0 \times 10^{-4}$	Roughness length of level ice	
$z_{0w}$	$3.27 \times 10^{-4}$	Roughness length of water upstream of the ice floe	
$s_l$	0.18	Attenuation parameter	





$c_{kw}$	0.2	Local form drag coefficient of oceanic form drag
$c_{fw}$	0.2	local form drag coefficient of ice floe edge form drag
$C_{sw}$	0.002	unobstructed skin drag
$c_{sf}$	0.2	geometrical parameter
$m_w$	10	Proportional parameter
$L_{min}$	8 (m)	Minimum ice floe size
$L_{max}$	300 (m)	Maximum ice floe size
β	0.75	Constant power

#### 485 code availability

490

495

500

505

The current version of the Large-scale roughness drag coefficient parameterization of HAMSOM-VICE v0.9 sea ice model is available from the project website <a href="https://zenodo.org/records/17054212">https://zenodo.org/records/17054212</a> under the Creative Commons Attribution 4.0 International licence. The exact version of the model of sea ice simulation in Bohai sea used to produce the results in this paper is archived on "The HAMSOM-VICE v0.9 sea ice model based on Large-scale roughness drag coefficient parameterization, scheme1" under DOI <a href="https://doi.org/10.5281/zenodo.17054212">https://doi.org/10.5281/zenodo.17054212</a> (Backhaus et al., 2025a).

The current version of the Small-scale roughness drag coefficient parameterization of HAMSOM-VICE v0.9 sea ice model is available from the project website <a href="https://zenodo.org/records/17054276">https://zenodo.org/records/17054276</a> under the Creative Commons Attribution 4.0 International licence. The exact version of the model of sea ice simulation in Bohai sea used to produce the results in this paper is archived on "The HAMSOM-VICE v0.9 sea ice model based on Small-scale roughness drag coefficient parameterization, scheme2" under DOI <a href="https://doi.org/10.5281/zenodo.17054276">https://doi.org/10.5281/zenodo.17054276</a> (Backhaus et al., 2025b).

The current version of the compilation and running script code is available from the project website <a href="https://zenodo.org/records/17063555">https://zenodo.org/records/17063555</a> under the Creative Commons Attribution 4.0 International licence. The exact version of the script used to produce the results in this paper is archived on "HAMSOM-VICE v0.9 compile and running" under DOI <a href="https://doi.org/10.5281/zenodo.17063555">https://doi.org/10.5281/zenodo.17063555</a> (Jia and Xu, 2025b).

The current version of the model result data postprocessing code is available from the project website <a href="https://zenodo.org/records/17060999">https://zenodo.org/records/17060999</a> under the Creative Commons Attribution 4.0 International licence. The exact version of the script used to produce the results in this paper is archived on "HAMSOM-VICE v0.9 result data processing code" under DOI <a href="https://doi.org/10.5281/zenodo.17060999">https://doi.org/10.5281/zenodo.17060999</a> (Jia and Xu, 2025c).

https://doi.org/10.5194/egusphere-2025-4290 Preprint. Discussion started: 20 November 2025

© Author(s) 2025. CC BY 4.0 License.



EGUsphere Preprint repository

The current version of the code used for processing the figures is available from the project website <a href="https://zenodo.org/records/17061378">https://zenodo.org/records/17061378</a> under the Creative Commons Attribution 4.0 International licence. The exact version of the script used to produce the results in this paper is archived on "Matlab\_sea\_ice\_plotting\_script" under DOI <a href="https://doi.org/10.5281/zenodo.17061378">https://doi.org/10.5281/zenodo.17061378</a> (Xu, 2025).

data availability

515

520

525

The current version of the input data including the forcing data, Initial Conditions, and bathymetry data is available from the project website <a href="https://zenodo.org/records/17063656">https://zenodo.org/records/17063656</a> under the Creative Commons Attribution 4.0 International licence. The exact version of the data used to produce the results in this paper is archived on "HAMSOM-VICE v0.9 input dataset, Bohai Sea 2011-2012" under DOI <a href="https://doi.org/10.5281/zenodo.17063656">https://doi.org/10.5281/zenodo.17063656</a> (Jia and Xu, 2025a).

The current version of the satellite data of total sea ice area in Bohai Sea from 2011 to 2012 is available from the project website <a href="https://zenodo.org/records/17055681">https://zenodo.org/records/17055681</a> under the Creative Commons Attribution 4.0 International licence. The exact version of the data used to produce the results in this paper is archived on "Satellite-data-of-total-sea-ice-area-in-Bohai-Sea-winter-2011-spring-2012" under DOI <a href="https://doi.org/10.5281/zenodo.17055681">https://doi.org/10.5281/zenodo.17055681</a> (Jia, 2025).

**Author contribution** 

B.J. and L.X. designed the study. L.X. and B.J. developed the model code, performed the simulations and conducted the formal analysis. X.C. and D.G. provided and processed the observational data. L.X. prepared the original draft. B.J. and Y.L. supervised the research and acquired funding. All authors reviewed and edited the manuscript.

**Competing interests** 

The authors declare that they have no conflict of interest.

Acknowledgements

Thanks to the "Tianhe EX" large-scale cluster provided by the National Supercomputing Center in Tianjin, which met the computing requirements of this research. We thank Dr. Thomas Pohlmann from the University of Hamburg, Germany, for providing the HAMSOM codes as well as for his helpful suggestions. We express our gratitude to the Generative Artificial Intelligence tools (AI). We declare that this tool was used solely to correct grammatical errors and enhance the clarity of the writing.

27





#### 535 References

- Arya, S. P. S.: Contribution of Form Drag on Pressure Ridges to the Air Stress on Arctic Ice, Journal of Geophysical Research, 78, 7092-7099, <a href="https://doi.org/10.1029/JC078i030p07092">https://doi.org/10.1029/JC078i030p07092</a>, 1973.
- Arya, S. P. S.: A drag partition theory for determining the large-scale roughness parameter and wind stress on the Arctic pack ice, Journal of Geophysical Research, 80, 3447-3454, <a href="https://doi.org/10.1029/JC080i024p03447">https://doi.org/10.1029/JC080i024p03447</a>, 1975.
- Backhaus, J.: Improved representation of topographic effects by a vertical adaptive grid in vector-ocean-model (VOM). Part I: Generation of adaptive grids, Ocean Modelling, 22, 114-127, <a href="https://doi.org/10.1016/j.ocemod.2008.02.003">https://doi.org/10.1016/j.ocemod.2008.02.003</a>, 2008. Backhaus, J. O.: A semi-implicit scheme for the shallow water equations for application to shelf sea modelling, Continental Shelf Research, 2, 243-254, <a href="https://doi.org/10.1016/0278-4343(82)90020-6">https://doi.org/10.1016/0278-4343(82)90020-6</a>, 1983.
  - Backhaus, J. O.: A three-dimensional model for the simulation of shelf sea dynamics, Deutsche Hydrografische Zeitschrift, 38, 165-187, https://doi.org/10.1007/BF02328975, 1985.
- 38, 165-187, <a href="https://doi.org/10.1007/BF02328975">https://doi.org/10.1007/BF02328975</a>, 1985.

  Backhaus, J. O., Reimer, M., and Mayer, B.: The HAMSOM-VICE v0.9 sea ice model based on Large-scale roughness drag coefficient parameterization, scheme1 (v1.0.1), Zenodo [code], <a href="https://doi.org/10.5281/zenodo.17054212">https://doi.org/10.5281/zenodo.17054212</a>, 2025a.

  Backhaus, J. O., Reimer, M., and Mayer, B.: The HAMSOM-VICE v0.9 sea ice model based on Small-scale roughness drag coefficient parameterization, scheme2 (v1.0.0), Zenodo [code], <a href="https://doi.org/10.5281/zenodo.17054276">https://doi.org/10.5281/zenodo.17054276</a>, 2025b.
- 550 Carton, J. A., Chepurin, G. A., and Chen, L.: SODA3: A New Ocean Climate Reanalysis, Journal of Climate, 31, 6967-6983, https://doi.org/10.1175/JCLI-D-18-0149.1, 2018. Castellani, G., Losch, M., Ungermann, M., and Gerdes, R.: Sea-ice drag as a function of deformation and ice cover: Effects simulated sea ice and ocean circulation in the Arctic. Ocean Modelling, https://doi.org/10.1016/j.ocemod.2018.06.002, 2018.
- Cole, S. T., Toole, J. M., Lele, R., Timmermans, M. L., Gallaher, S. G., Stanton, T., Shaw, W. J., Hwang, B., Maksym, T., Wilkinson, J. P., Ortiz, M., Graber, H. C., Rainville, L., Petty, A. A., Farrell, S. L., Richter-Menge, J., and Haas, C.: Ice and ocean velocity in the Arctic marginal ice zone: Ice roughness and momentum transfer, 5, 55, <a href="https://doi.org/10.1525/elementa.241">https://doi.org/10.1525/elementa.241</a>, 2017.
  - Crameri, F.: Scientific colour maps (8.0.1), <a href="https://doi.org/10.5281/zenodo.8409685">https://doi.org/10.5281/zenodo.8409685</a>, 2023.
- Davis, N. R. and Wadhams, P.: A statistical analysis of Arctic pressure ridge morphology, Journal of Geophysical Research, 100, 10915-10925, <a href="https://doi.org/10.1029/95JC00007">https://doi.org/10.1029/95JC00007</a>, 1995.
   Donlon, C., Martin, M. J., Stark, J. D., Roberts-Jones, J., Fiedler, E. K., and Wimmer, W.: The Operational Sea Surface Temperature and Sea Ice Analysis (OSTIA) system, Remote Sensing of Environment, 116, 140-158, <a href="https://doi.org/10.1016/j.rse.2010.10.017">https://doi.org/10.1016/j.rse.2010.10.017</a>, 2012.
- Erofeeva, L., Padman, L., and Howard, S.: Tide model driver (TMD) version 2.5, toolbox for matlab, Earth & Space Research (ESR) [dataset], 2020.
  - Gu, W., Liu, C., Yuan, S., Li, N., Chao, J., Li, L., and Xu, Y.: Spatial distribution characteristics of sea-ice-hazard risk in Bohai, China, Annals of Glaciology, 54, 73 79, https://doi.org/10.3189/2013AoG62A303, 2013.
- Guo, W., Zhang, S., and Wu, G.: Quantitative oil spill risk from offshore fields in the Bohai Sea, China, The Science of the total environment, 688, 494-504, https://doi.org/10.1016/j.scitotenv.2019.06.226, 2019.
  - Hanssen-Bauer, I. and Gjessing, Y. T.: Observations and model calculations of aerodynamic drag on sea ice in the Fram Strait, Tellus Series A-dynamic Meteorology & Oceanography, 40A, 151-161, <a href="https://doi.org/10.3402/TELLUSA.V40I2.11789">https://doi.org/10.3402/TELLUSA.V40I2.11789</a>, 1988.
- Harder, M.: Roughness, age and drift trajectories of sea ice in large-scale simulations and their use in model verifications, Annals of Glaciology, 25, 237 240, <a href="https://doi.org/10.3189/S0260305500014105">https://doi.org/10.3189/S0260305500014105</a>, 1997.
- Hartmann, J., Kottmeier, C., and Wamser, C.: Radiation and Eddy Flux Experiment 1991 (REFLEX I), Alfred-Wegener-Institut für Polar- und Meeresforschung;, Bremerhaven, Germany0176-5027, 1-72, <a href="https://doi.org/10.2312/BzP\_0105\_1992">https://doi.org/10.2312/BzP\_0105\_1992</a>, 1992.
- Hibler III, W. D., Weeks, W. F., and Mock, S. J.: Statistical aspects of sea-ice ridge distributions, Journal of Geophysical Research, 77, 5954-5970, https://doi.org/10.1029/JC077i030p05954, 1972.
- Hibler, W. D.: A Dynamic Thermodynamic Sea Ice Model, Journal of Physical Oceanography, 9, 815-846, https://doi.org/10.1175/1520-0485(1979)009<0815:ADTSIM>2.0.CO;2, 1979.





- Holland, D. M. and Jenkins, A.: Modeling Thermodynamic Ice–Ocean Interactions at the Base of an Ice Shelf, Journal of Physical Oceanography, 29, 1787-1800, <a href="https://doi.org/10.1175/1520-0485(1999)029">https://doi.org/10.1175/1520-0485(1999)029</a><1787:MTIOIA>2.0.CO;2, 1999.
- Ji, S.: Numerical simulation of Bohai sea ice and engineering applications, Dalian University Of Technology, 2001.

  Jia, B.: Satellite-data-of-total-sea-ice-area-in-Bohai-Sea-winter-2011-spring-2012 (v1), Zenodo [dataset], <a href="https://doi.org/10.5281/zenodo.17055681">https://doi.org/10.5281/zenodo.17055681</a>, 2025.
  - Jia, B. and Chen, X. e.: Application of an ice-ocean coupled model to Bohai Sea ice simulation, Journal of Oceanology and Limnology, 39, 1-13, <a href="https://doi.org/10.1007/s00343-020-9168-8">https://doi.org/10.1007/s00343-020-9168-8</a>, 2020.
- 590 Jia, B. and Xu, L.: HAMSOM-VICE v0.9 input dataset, Bohai Sea 2011-2012 (v1), Zenodo [dataset], <a href="https://doi.org/10.5281/zenodo.17063656">https://doi.org/10.5281/zenodo.17063656</a>, 2025a.
  - Jia, B. and Xu, L.: HAMSOM-VICE v0.9 compile and running (v1), Zenodo [code], <a href="https://doi.org/10.5281/zenodo.17063555">https://doi.org/10.5281/zenodo.17063555</a>, 2025b.
  - Jia, B. and Xu, L.: HAMSOM-VICE v0.9 result data processing code (v1), Zenodo [code], https://doi.org/10.5281/zenodo.17060999, 2025c.
  - Jia, B., Chen, X. e., and Zheng, P.: The role of the heat exchange coefficient at the ice/ocean interface in Bohai Sea ice modeling, Continental Shelf Research, 241, 104735, <a href="https://doi.org/10.1016/j.csr.2022.104735">https://doi.org/10.1016/j.csr.2022.104735</a>, 2022.
  - Jia, B., Xu, L., Chen, X., and Zhang, W.: Spatio-temporal variations of the heat fluxes at the ice-ocean interface in the Bohai Sea, Frontiers in Marine Science, Volume 11 2024, https://doi.org/10.3389/fmars.2024.1471061, 2024.
- Johannessen, O. M.: Note on some vertical profiles below ice floes in the Gulf of St. Lawrence and near the North Pole, 75, 2857-2761, <a href="https://doi.org/10.1029/JC075i015p02857">https://doi.org/10.1029/JC075i015p02857</a>, 1970.
  - Kawaguchi, Y., Hoppmann, M., Shirasawa, K., Rabe, B., and Kuznetsov, I.: Dependency of the drag coefficient on boundary layer stability beneath drifting sea ice in the central Arctic Ocean, Scientific Reports, 14, 15446, https://doi.org/10.1038/s41598-024-66124-8, 2024.
- Kovacs, A.: On the structure of pressured sea ice, Cold Regions Research and Engineering Laboratory (CRREL)CRREL-IR-137, <a href="https://doi.org/10.21236/ad0722784">https://doi.org/10.21236/ad0722784</a>, 1970.
  - Lu, P., Li, Z., Cheng, B., and Leppranta, M.: A parameterization of the ice-ocean drag coefficient, Journal of Geophysical Research Atmospheres, 116, https://doi.org/10.1029/2010JC006878, 2011.
  - Lüpkes, C. and Birnbaum, G.: Surface Drag in the Arctic Marginal Sea-ice Zone: A Comparison of Different Parameterisation Concepts, Boundary-Layer Meteorology, 117, 179-211, https://doi.org/10.1007/S10546-005-1445-8, 2005.
- 610 Concepts, Boundary-Layer Meteorology, 117, 179-211, <a href="https://doi.org/10.1007/S10546-005-1445-8">https://doi.org/10.1007/S10546-005-1445-8</a>, 2005. Lüpkes, C., Gryanik, V. M., Rösel, A., Birnbaum, G., and Kaleschke, L.: Effect of sea ice morphology during Arctic summer on atmospheric drag coefficients used in climate models, Geophysical Research Letters, 40, 446-451, <a href="https://doi.org/10.1002/grl.50081">https://doi.org/10.1002/grl.50081</a>, 2012.
- Madsen, O. S. and Bruno, M. S.: A Methodology for the Determination of Drag Coefficients for Ice Floes, Journal of Offshore Mechanics and Arctic Engineering, 109, 381-387, https://doi.org/10.1115/1.3257035, 1987.
- Mai, S., Wamser, C., and Kottmeier, C.: Geometric and aerodynamic roughness of sea ice, Boundary-Layer Meteorology, 77, 233-248, https://doi.org/10.1007/BF00123526, 1996.
  - Martinson, D. G. and Wamser, C.: Ice drift and momentum exchange in winter Antarctic pack ice, Journal of Geophysical Research Atmospheres, 95, 1741-1755, <a href="https://doi.org/10.1029/JC095IC02P01741">https://doi.org/10.1029/JC095IC02P01741</a>, 1990.
- 620 Mcphee, M. G.: The Effect of the Oceanic Boundary Layer on the Mean Drift of Pack Ice: Application of a Simple Model, Journal of Physical Oceanography, 9, 388-400, <a href="https://doi.org/10.1175/1520-0485(1979)009">https://doi.org/10.1175/1520-0485(1979)009</a><0388:TEOTOB>2.0.CO;2, 1979. Mcphee, M. G.: Turbulent Heat Flux in the Upper Ocean Under Sea Ice, Journal of Geophysical Research, 97, 5365-5379, <a href="https://doi.org/10.1029/92JC00239">https://doi.org/10.1029/92JC00239</a>, 1992.
- Mcphee, M. G.: The sea ice-ocean boundary layer, in: Sea Ice, 3rd ed., Wiley-Blackwell, Chichester, UK, 138-159, https://doi.org/10.1002/9781118778371.CH5, 2017.
- Mcphee, M. G. and Smith, J. D.: Measurements of the Turbulent Boundary Layer under Pack Ice, Journal of Physical Oceanography, 6, 696-711, <a href="https://doi.org/10.1175/1520-0485(1976)006">https://doi.org/10.1175/1520-0485(1976)006</a></a></a>0696:MOTTBL>2.0.CO;2, 1976.

  Mock, S. J., Hartwell, A. D., and Hibler, W. D.: Spatial aspects of pressure ridge statistics, Journal of Geophysical Research,
  - 77, 5945-5953, https://doi.org/10.1029/JC077i030p05945, 1972.
- Ning, X., Xueqin, L., Shuai, Y., Yuxian, M., Wenqi, S., and Weibin, C.: Sea ice disaster risk assessment index system based on the life cycle of marine engineering, Natural Hazards, 95, 445-462, <a href="https://doi.org/10.1007/s11069-018-3463-0">https://doi.org/10.1007/s11069-018-3463-0</a>, 2018.



665



- Olason, E.: A dynamical model of Kara Sea land-fast ice, Journal of Geophysical Research: Oceans, 121, 3141-3158, <a href="https://doi.org/10.1002/2016JC011638">https://doi.org/10.1002/2016JC011638</a>, 2016.
- Ólason, E. Ö. and Harms, I.: Polynyas in a dynamic-thermodynamic sea-ice model, The Cryosphere, 4, 147-160, https://doi.org/10.5194/tc-4-147-2010, 2010.
  - Overland, J. E. and Colony, R. L.: Geostrophic drag coefficients for the central Arctic derived from Soviet drifting station data, Tellus A, 46, 75-85, https://doi.org/10.3402/TELLUSA.V46I1.15436, 1994.
  - Overland, J. E. and Davidson, K. L.: Geostrophic drag coefficients over sea ice, Tellus A, 44, 54-66, <a href="https://doi.org/10.3402/TELLUSA.V44I1.17118">https://doi.org/10.3402/TELLUSA.V44I1.17118</a>, 1992.
- Pease, C. H., Salo, S. A., and Overland, J. E.: Drag measurements for first-year sea ice over a shallow sea, Journal of Geophysical Research, 88, 2853-2862, <a href="https://doi.org/10.1029/JC088IC05P02853">https://doi.org/10.1029/JC088IC05P02853</a>, 1983.
  - Rothrock, D. A.: The energetics of the plastic deformation of pack ice by ridging, Journal of Geophysical Research, 80, 4514-4519, <a href="https://doi.org/10.1029/JC080I033P04514">https://doi.org/10.1029/JC080I033P04514</a>, 1975.
- Rothrock, D. A. and Thorndike, A. S.: Geometric properties of the underside of sea ice, Journal of Geophysical Research, 85, 3955-3963, <a href="https://doi.org/10.1029/JC085IC07P03955">https://doi.org/10.1029/JC085IC07P03955</a>, 1980.
- Saha, S., Moorthi, S., Wu, X., Wang, J., Nadiga, S., Tripp, P., Behringer, D., Hou, Y.-T., Chuang, H.-Y., Iredell, M., Ek, M. B., Meng, J., Yang, R., Mendez, M. P., Dool, H. v. d., Zhang, Q., Wang, W., Chen, M., and Becker, E. J.: NCEP Climate Forecast System Version 2 (CFSv2) Selected Hourly Time-Series Products (Version 2), Research Data Archive at the National Center for Atmospheric Research, Computational and Information Systems Laboratory [dataset], https://doi.org/10.5065/D6N877VB, 2011.
- Semtner, A. J.: A Model for the Thermodynamic Growth of Sea Ice in Numerical Investigations of Climate, Journal of Physical Oceanography, 6, 379-389, https://doi.org/10.1175/1520-0485(1976)006<0379:AMFTTG>2.0.CO;2, 1976.
  - Shi, Y., Yang, Y., Teng, Y., Sun, M., and Yun, S.: Mechanism of sea ice formation based on comprehensive observation data in Liaodong Bay, China, Journal of Oceanology and Limnology, 37, 1846-1856, <a href="https://doi.org/10.1007/s00343-019-8269-8">https://doi.org/10.1007/s00343-019-8269-8</a>, 2019.
- 655 2019.
  Steele, M., Morison, J., and Untersteiner, N.: The partition of air-ice-ocean momentum exchange as a function of ice concentration, floe size, and draft, Journal of Geophysical Research, 94, 12739-12750, https://doi.org/10.1029/JC094IC09P12739, 1989.
- Steiner, N.: Introduction of variable drag coefficients into sea-ice models, Annals of Glaciology, 33, 181 186, https://doi.org/10.3189/172756401781818149, 2001.
- Steiner, N., Harder, M., and Lemke, P.: Sea-ice roughness and drag coefficients in a dynamic–thermodynamic sea-ice model for the Arctic, Tellus A. 51, 964-978, https://doi.org/10.1034/J.1600-0870.1999.00029.X. 1999.
  - Sterlin, J., Tsamados, M., Fichefet, T., Massonnet, F., and Barbic, G.: Effects of sea ice form drag on the polar oceans in the NEMO-LIM3 global ocean—sea ice model, Ocean Modelling, 184, 102227, <a href="https://doi.org/10.1016/j.ocemod.2023.102227">https://doi.org/10.1016/j.ocemod.2023.102227</a>, 2023
  - Su, J., Wu, H., Zhang, Y., and Liu, Q.: Study of an Ice-ocean Coupled Model For a Regional Sea the Bohai Sea, The Thirteenth International Offshore and Polar Engineering Conference, ISOPE-I-03-079, 2003.
  - SU, J., WU, H., ZHANG, Y., LIU, Q., and BAI, S.: A coupled ice-ocean model for the Bohai Sea I. Study on model and parameter, Acta oceanologica sinica, 23, 597-608, 2004.
- 670 SU, J., WU, H., ZHANG, Y., LIU, Q., and BAI, S.: A coupled ice- ocean model for the Bohai Sea II. Case study, Acta Oceanologica Sinica, 24, 54-67, 2005.
  - Timco, G. W. and Burden, R.: An analysis of the shapes of sea ice ridges, Oceanographic Literature Review, 25, 65-77, <a href="https://doi.org/10.1016/S0165-232X(96)00017-1">https://doi.org/10.1016/S0165-232X(96)00017-1</a>, 1997.
- Tsamados, M., Feltham, D. L., Schroeder, D., Flocco, D., Farrell, S. L., Kurtz, N., Laxon, S. W., and Bacon, S.: Impact of Variable Atmospheric and Oceanic Form Drag on Simulations of Arctic Sea Ice, Journal of Physical Oceanography, 44, 1329-1353, <a href="https://doi.org/10.1175/JPO-D-13-0215.1">https://doi.org/10.1175/JPO-D-13-0215.1</a>, 2014.
  - Wang, K., Wang, C., and Wu, H.: Treatment of the Thermal Process of Seawater in the Bohai Sea, Marine Science Bulletin, 1-11, 2000.
- Wang, R., Liu, X., and Zhang, L.: A Numerical Experiment on the Seawater of the Bohai Sea, Acta Oceanologica Sinica (Chinese Edition), 572-580, 1984.
  - Xu, L.: Matlab sea ice plotting script (v1), Zenodo [code], https://doi.org/10.5281/zenodo.17061378, 2025.





Yan, Y., Gu, W., Xu, Y., and Li, Q.: The in situ observation of modelled sea ice drift characteristics in the Bohai Sea, Acta Oceanologica Sinica, 38, 17-25, <a href="https://doi.org/10.1007/s13131-019-1395-5">https://doi.org/10.1007/s13131-019-1395-5</a>, 2019.

Zhang, D.-y. and Yue, Q.: Major challenges of offshore platforms design for shallow water oil and gas field in moderate ice conditions, Ocean Engineering, 38, 1220-1224, <a href="https://doi.org/10.1016/J.OCEANENG.2011.05.012">https://doi.org/10.1016/J.OCEANENG.2011.05.012</a>, 2011.

Zweng, M. M., Reagan, J. R., Seidov, D., Boyer, T. P., Locarnini, R. A., Garcia, H. E., Mishonov, A. V., Baranova, O. K., Weathers, K. W., Paver, C. R., and Smolyar, I. V.: World Ocean Atlas 2018, Volume 2: Salinity, 2, 50-82, https://doi.org/10.25923/9pgv-1224, 2019.

690

685